FastIsostasy v1.0 – An accelerated regional GIA model accounting for the lateral variability of the solid Earth

Jan Swierczek-Jereczek[1, 2], Marisa Montoya[1, 2], Konstantin Latychev[3], Alexander Robinson[4], Jorge Alvarez-Solas[1, 2], and Jerry Mitrovica[5]

[1]Department of Earth Physics and Astrophysics, Complutense University of Madrid, Madrid, Spain.
[2]Geosciences Institute, CSIC-UCM, Madrid, Spain.
[3]Seakon, Toronto, Canada.
[4]Alfred Wegener Institute, Helmholtz Centre for Polar and Marine Research, Potsdam, Germany.
[5]Department of Earth and Planetary Sciences, Harvard University, Massachusetts, USA.

Correspondence: Jan Swierczek-Jereczek (janswier@ucm.es)

Abstract. The vast majority of ice-sheet modelling studies rely on simplified representations of the Glacial Isostatic Adjustment (GIA), which, among other limitations, do not account for lateral variations of the lithospheric thickness and upper-mantle viscosity. In studies using 3D GIA models, this has however been shown to have major impacts on the dynamics of marine-based sectors of Antarctica, which are likely to be the greatest contributors to sea-level rise in the coming centuries. This gap

5 in comprehensiveness is explained by the fact that 3D GIA models are computationally expensive, seldomly open-source and require the implementation of an iterative coupling scheme to converge with the history of the ice-sheet model. To close this gap between "best" and "tractable" GIA models, we here propose FastIsostasy, a regional GIA model capturing lateral variations of the lithospheric thickness and mantle viscosity. By means of Fast-Fourier transforms and a hybrid collocation scheme to solve its underlying partial differential equation, FastIsostasy can simulate 100,000 years of high-resolution bedrock displacement

10 in only minutes of single-CPU computation, including the changes in sea-surface height due to mass redistribution. Despite its 2D grid, FastIsostasy parametrises the depth-dependent viscosity in a physically meaningful way and therefore represents the depth dimension to a certain extent. FastIsostasy is here benchmarked against analytical, 1D and 3D GIA solutions and shows very good agreement with them. It is fully open-source, documented with many examples and provides a straight-forward interface for coupling to an ice-sheet model. The model is benchmarked here based on its implementation in Julia, while a

15 Fortran version is also provided to allow for compatibility with most existing ice-sheet models. The Julia version provides additional features, including a vast library of time-stepping methods and GPU support.

1 Introduction

Glacial isostatic adjustment (GIA) denotes the crustal displacement that results from changes in the ice, liquid water and sedi-
ment columns, as well as associated changes in Earth's gravity and rotation axis (Mitrovica et al., 2001), ultimately impacting
the sea level (Farrell and Clark, 1976). In the present work, we focus on the deformation and gravitational effects. The former is
a net negative feedback on ice-sheet mass balance through the lapse rate of the troposphere and both imply additional negative
feedbacks on ice-sheet dynamics in the case of marine-based regions (Gomez et al., 2010, 2012, 2015, 2018; Whitehouse et al.,
2019). Although enhanced melting at the grounding line results in a grounding-line retreat, it also implies a regional bedrock
uplift and a reduction of the sea-surface height, respectively due to the reduced load and gravitational pull of the ice sheet on
the oceans. As depicted in Fig. 1, these effects combine in a decrease in sea level and a potential readvance of the grounding
line, therefore conditioning the marine ice-sheet instability along with the buttressing effect from ice shelves (Gudmundsson
et al., 2012). It was shown that the representation of the deformation and gravitational feedbacks can stabilise grounding lines
on retrograde slopes (Gomez et al., 2010, 2012) and that a rapid bedrock uplift can prevent the collapse of marine-terminating
glaciers that are transiently forced (Konrad et al., 2014, 2015, 2016). Furthermore, an uplifting bedrock might lead isolated
bathymetric peaks to connect with the ice sheet, creating so-called pinning points (Adhikari et al., 2014). Although the negative
feedbacks are illustrated here for ice-sheet retreat, they conversely apply to ice-sheet growth.

For a given load applied to the solid Earth, the amplitude, time scale and pattern of the bedrock deformation are determined
by the upper-mantle density and viscosity and the lithospheric thickness. These parameters are close to being laterally homo-
geneous in many regions of the solid Earth, which motivated the development of 1D GIA models, where these parameters only
depend on the depth coordinate. However, some regions are an exception to this and present a significant lateral variability
of solid-Earth parameters (further simply referred to as LV), even on relatively short spatial scale. Since Antarctica displays a
strong dichotomy between a moderately rifting system in the West and an old craton in the East (Behrendt, 1999), it represents
a prototypical example of LV. As depicted in Fig. 2, the lithospheric thickness and upper-mantle viscosity are respectively as
little as $50\,\mathrm{km}$ and $10^{18}\,\mathrm{Pa\,s}$ in the West and as large as $250\,\mathrm{km}$ and $10^{23}\,\mathrm{Pa\,s}$ in the East (Morelli and Danesi, 2004; Nield
et al., 2014; Lloyd et al., 2015, 2020; Barletta et al., 2018; Whitehouse et al., 2019; Wiens et al., 2022; Ivins et al., 2022). For
simulations of the Antarctic Ice Sheet (AIS) on the time scale of glacial cycles, accounting for the Antarctic LV by using 3D
GIA models has shown great differences compared to 1D GIA models (Gomez et al., 2018; Van Calcar et al., 2023), leading to
discrepancies reaching up to $700\,\mathrm{km}$ for the grounding line position and more than $1\,\mathrm{km}$ for the ice thickness. Although these
impacts are large, they are to be expected, given that the AIS is characterised by large marine-based regions - the East-Antarctic
basins and the West-Antarctic Ice-Sheet (WAIS), with respective sea-level contributions from ice grounded below sea level of
about $19.2\,\mathrm{m}$ and $3.4\,\mathrm{m}$ (Fretwell et al., 2013) - whose evolution strongly depends on the representation of the GIA feedbacks
depicted in Fig. 1. While both regions are likely to present abrupt transitions to ice-free conditions under warming scenarios,
the WAIS is thought to have particularly low resilience, displaying a bifurcation at a mean global warming of as little as $2°\mathrm{C}$
with respect to pre-industrial era (Garbe et al., 2020). In the context of anthropogenic warming, this is very likely to result in an
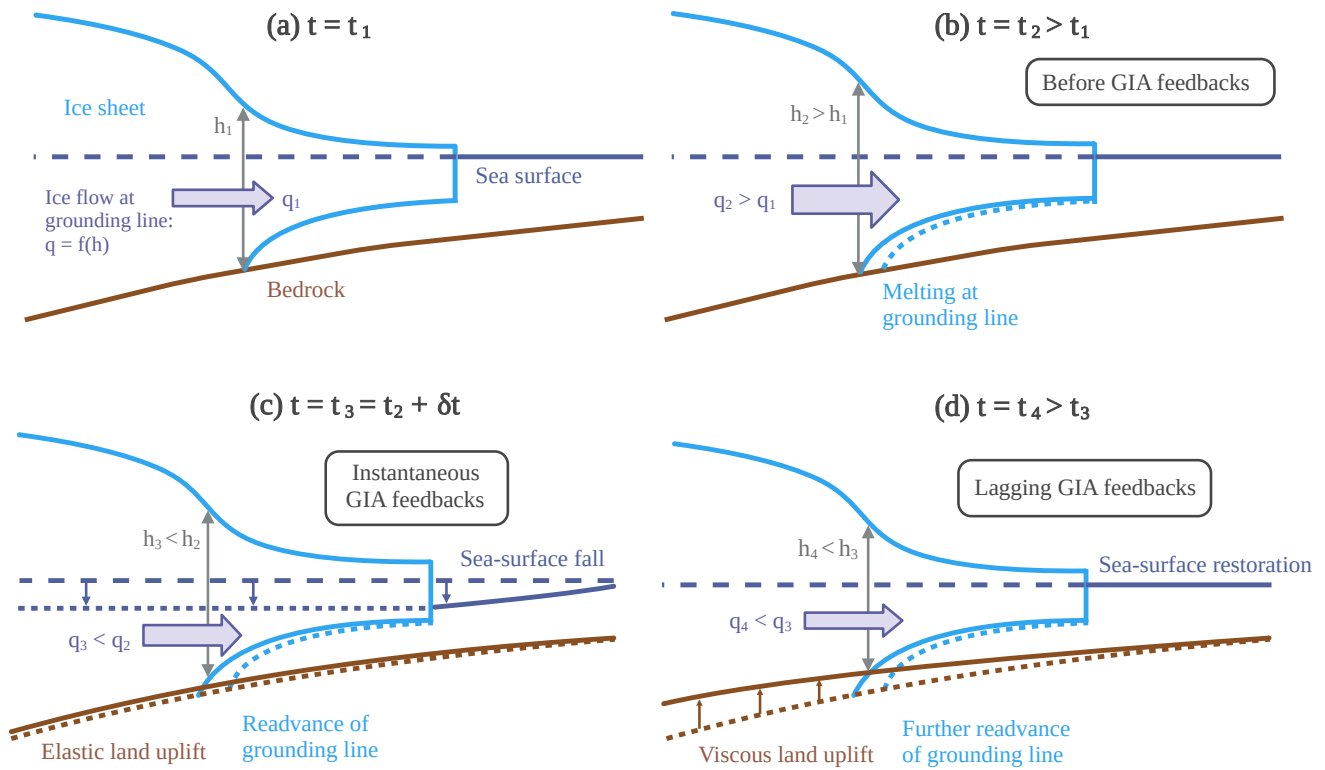
Figure 1. Idealised representation, adapted from (Whitehouse et al., 2019), of the negative GIA feedbacks at a marine-terminating glacier on a retrograde bedrock (e.g. Gomez et al., 2010). We perturb the (a) initial configuration of the ice-sheet by (b) enhanced melting at the grounding line, leading to larger thickness, and therefore increased outflow, at the grounding line. (c) The loss of ice leads to an instantaneous ($\delta t \ll 1\,\mathrm{yr}$) decrease of the local sea level, which can be decomposed into an elastic uplift of the bedrock, and a decrease of the sea-surface height due to the reduction of the gravitational pull on the ocean, leading to a readvance of the grounding line. (d) The elastic uplift is followed by a larger, viscous uplift which further readvances the grounding line and compensates the mass anomaly generated by the ice loss, therefore restoring the sea-surface height close to its original value.

unprecedented rate of sea-level rise, challenging the adaptation of coastal livelihoods that represent a large portion of human societies (Kulp and Strauss, 2019).

For these reasons, comprehensive projections of sea-level rise require the representation of the Antarctic LV in coupled ice-sheet/GIA settings. Furthermore, the upper-mantle viscosity is uncertain and involves discrepancies of up to two orders of
55 magnitude at some locations, depending on how viscosities are inferred from sparse seismic data (Ivins et al., 2022). Parametric uncertainties of the ice-sheet and GIA models thus need to be propagated to the solution, typically by means of ensemble simulations. However, this is not a standard practice in ice-sheet modelling, mostly due to the sheer computational cost of using

3D GIA models and the fact that none of them is fully open-source to this date - some of them even requiring a commercial licence. Instead, the vast majority of ice-sheet simulations rely on greatly simplified GIA models without accounting for the parametric uncertainties of the solid Earth, thus potentially introducing biases in sea-level projections (Gomez et al., 2015). This also holds to a certain extent for the Ice-Sheet Model Intercomparison Project (ISMIP) (Seroussi et al., 2020), used as the physical basis for the reports of the Intergovernmental Panel on Climate Change (IPCC). In summary, the ice-sheet modelling community faces the somewhat paradoxical situation of being well aware of how important 3D GIA is, without being able to represent it at a reasonable computational cost.
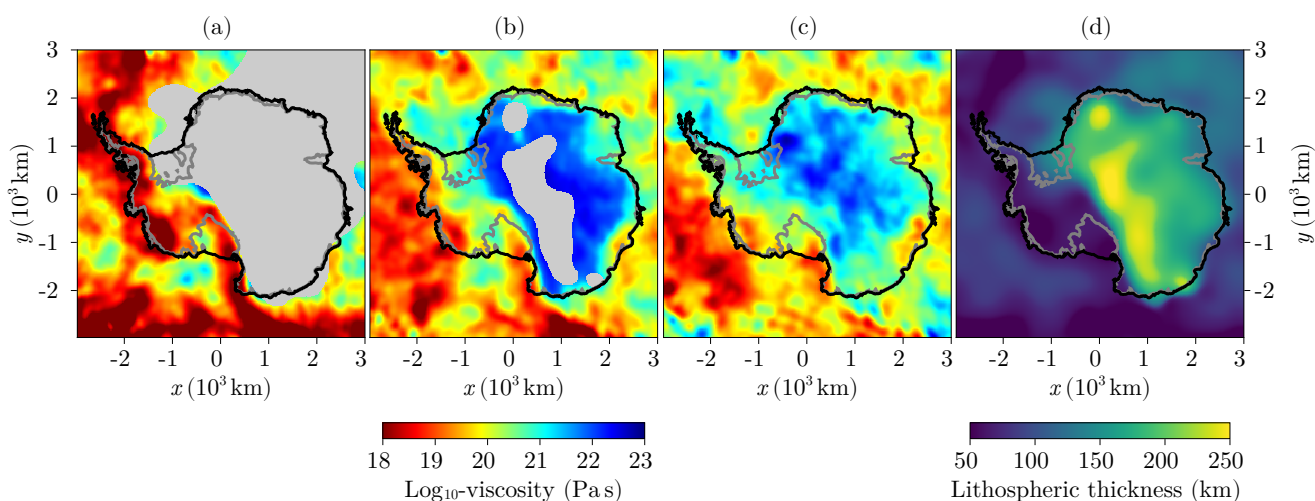
Figure 2. (a-c) Upper-mantle viscosity from (Whitehouse et al., 2019; Ivins et al., 2022) at 100, 200 and 300 km depth, respectively. If the lithospheric thickness (Pan et al., 2022), depicted in (d), is larger than the layer depth, a grey shading is applied. The black and dark grey contour lines respectively indicate the present-day ice and grounded ice margins (Morlighem et al., 2020).

To tackle this, we here propose FastIsostasy, a regional GIA model derived from first principles and specially tailored for the needs of ice-sheet modellers. FastIsostasy (1) accounts for LV, (2) allows for the depth-dependence of the mantle viscosity, (3) captures the dependence of the response time scale on the spatial scale of the load, (4) approximates the sea-level evolution, (5) is computationally cheap, (6) is extensively tested and (7) offers a simple, open-source and documented interface for an effortless coupling to an ice-sheet model. To illustrate its capabilities, Antarctica is used as leitmotif of the present work since it displays (a) a high LV and depth-dependence of solid-Earth parameters as depicted in Fig. 2, (b) a high sensitivity to GIA due to the vast marine sectors of the AIS, (c) a large impact on the future of human societies due to possible rapid sea-level rise and (d) large uncertainties in the solid-Earth parameters due, in part, to limited regional data sets. Antarctica might therefore be "the toughest test" when it comes to GIA modelling. We emphasise that, because of this, the tools provided here are equally well applicable to any other region covered by a past, present or future ice sheet.

FastIsostasy in the model hierarchy

The hierarchy of GIA models displays a large gap between the regional models, largely used by the ice-sheet modelling community, and the global models, developed by the GIA community. We herein give a brief overview, summarised in Table 1, of the GIA model classes that are available to date. We focus on Maxwell rheology, since it is the only one that is sufficiently constrained in literature. We start with the lowest and end with the highest model complexity:

- **ELRA:** We here propose to rename the Elastic-Lithosphere/Relaxed-Asthenosphere (ELRA) (Le Meur and Huybrechts, 1996) to Elastic-Lithosphere/Relaxed-mAntle without any change in the acronym to avoid confusions. This is motivated by the fact that, in cratonic regions with a thick lithosphere, as e.g. East-Antarctica, there might be no asthenosphere. ELRA conceptualises the structure of the solid Earth as two layers stacked along the depth dimension of a Cartesian coordinate system, obtained by a regional projection of the spherical Earth. The elastic lithosphere is parametrised by its thickness $T = \mathrm{constant}$ and undergoes instantaneous compression under the effect of a load. It is underlain by the upper mantle, a viscous half-space parametrised by a constant the relaxation time τ, with which the solution exponentially converges to the equilibrium solution. This parametrisation is however simplistic, since, in reality, the response time scale of the solid Earth does not only depend on the viscosity, but also on the transient behaviour of the neighbouring points and the wavenumber of the load. Furthermore, ELRA does not represent the depth-dependence of the mantle viscosity nor any LV, and ignores the gravitational and rotational feedbacks on the sea level. In Konrad et al. (2014), ELRA was demonstrated to display important transient differences to a 1D GIA model as well as large discrepancies in the representation of the peripheral forebulge. Despite these numerous flaws, ELRA remains the standard choice for ice-sheet modellers, as it mimics the visco-elastic behaviour of the solid Earth with little implementation effort and low computational cost.

- **ELVA:** This modelling approach was proposed by Cathles (1975), applied to ice-sheet modelling for the first time in Lingle and Clark (1985) and efficiently implemented in Bueler et al. (2007) by means of a Fourier collocation method (FCM). Although this model is sometimes named after the authors of the aforementioned work, we here try to provide a unifying terminology and therefore call it Elastic-Lithosphere/Viscous-mAntle (ELVA). ELVA resembles ELRA in its structure but is parametrised by the spatially homogeneous upper-mantle viscosity η. It thus avoids any conversion from viscosity to relaxation time and allows the mechanical response to depend on the wavelength of the load (Bueler et al., 2007). Furthermore, it permits embedding more of the radial structure of the mantle viscosity by introducing a viscous channel between the elastic plate and the viscous half-space. However, it does not address any other limitation of ELRA.

- **LV-ELRA:** The laterally-variable ELRA (LV-ELRA) proposed in (Coulon et al., 2021) is conceptually similar to ELRA but allows for laterally-variable upper-mantle relaxation time $\tau(x,y)$ and lithospheric thickness $T(x,y)$. The latter is achieved by solving equations derived from thin plate theory (Ventsel and Krauthammer, 2001; Coulon et al., 2021). A smoothing of the $\tau(x,y)$ field is typically performed to preserve a certain spatial coherence of the transient dynamics of

the vertical deformation, i.e. neighbouring points have similar time scales. Although this is a generalisation of ELRA, it does not address its many other limitations.

- **1D GIA:** Self-gravitating visco-elastic Earth models, commonly called 1D GIA models, capture the radial structure of the solid Earth and compute its vertical and horizontal deformation by means of spherical harmonics. They typically represent the spatial heterogeneity of the sea-surface height, the migration of shorelines and the rotational feedback (Mitrovica and Milne, 2003; Kendall et al., 2005; Spada and Melini, 2019). Most of them were cross-validated in Spada et al. (2011) and Martinec et al. (2018), showing great agreement while presenting intermediate computational cost. However, they are incapable of rendering any LV (e.g. Klemann et al., 2008; Spada and Melini, 2019).

- **3D GIA:** 3D GIA models account for all the processes represented in 1D GIA models and are, in addition, capable of fully capturing the heterogeneity of solid Earth parameters. Unlike 1D GIA models, they were not coherently benchmarked so far but can be considered to be the best technology available for cases like Antarctica. They either rely on spherical harmonics (e.g. Bagge et al., 2021), finite elements (e.g. Wu, 2004), finite volumes (e.g. Latychev et al., 2005; Gomez et al., 2018), or perturbation theory (e.g. Wu and Wang, 2006; Zhong et al., 2022). Simulations on glacial time scales however typically require from days up to weeks of computation, even with heavily parallelised codes (Gomez et al., 2018; Van Calcar et al., 2023). This is particularly problematic for propagating parametric uncertainties of the solid Earth and the ice-sheet on long simulation times, since the limit of computational resources is reached with only a few ensemble members. Furthermore, 3D GIA models tend to have large time steps $\Delta t_{\mathrm{GIA}} \in [100, 1000]\,\mathrm{yr}$ compared to ice-sheet models $\Delta t_{\mathrm{ISM}} \in [1, 10]\,\mathrm{yr}$. In case of a two-way coupling, an iterative procedure has to be implemented for the history of both components to converge (Van Calcar et al., 2023; Wan et al., 2022).

Although computing the changes in sea-surface height requires, a-priori, a global domain, it can also be approximated on a regional one. This was done in Coulon et al. (2021) and combined with an LV-ELRA. The so-called *elementary GIA model* obtained this way represents one of the highest complexity of regional GIA models to this date and a valuable improvement for regional modelling, as it bypasses the computational expense of 1D or 3D GIA models. Going a step further in the complexity of regional models, ASPECT has recently been extended and offers an open-source solution to compute the deformational response on laterally-variable Earth structures (Weerdesteijn et al., 2023). It is the first regional GIA model to fully resolve the depth dimension down to the core-mantle boundary and allows for grid refinement in regions where a higher resolution is needed. Despite great efforts on parallelism, ASPECT requires about an hour to compute a few hundred years of high-resolution bedrock deformation on 256 CPUs. This represents a computational cost that is too high for most on-going ice-sheet modelling studies, while ignoring the gravitational effects of GIA and the treatment of the sea level.

This essentially means that no regional model is able to compute a comprehensive GIA response subject to LV within a run time that is acceptable for modelling ice sheets on the time scale of glacial cycles. To fill the complexity gap between regional and 3D GIA models, we introduce FastIsostasy in the next section. It essentially consists of a laterally-variable ELVA (LV-ELVA) model coupled to the regional sea-level model (ReSeLeM). Subsequently, we discuss some of the practical features of the Julia implementation, such as the adaptive time stepping for integration and GPU support. Finally, we benchmark

	ELRA	**ELVA**	**Elementary GIA model** (LV-ELRA)	**FastIsostasy** (LV-ELVA)	**1D GIA**	**3D GIA**
Rheology	Maxwell-like	Maxwell	Maxwell-like	Maxwell	Maxwell	Maxwell and others
Explicit mantle viscosity	×	✓	×	✓	✓	✓
Wavelength-dependent response	×	✓	×	✓	✓	✓
LV	×	×	≃	✓	×	✓
Radial structure	2 layers (lumped)	3 layers (lumped)	2 layers (lumped)	n layers (lumped)	n layers (resolved)	n layers (resolved)
Domain	regional	regional	regional	regional	global	global
Distortion accounted for	×	×	×	✓	✓	✓
Gravitationally self-consistent	×	×	×	×	✓	✓
Sea level	×	×	≃	≃	✓	✓
Time-varying ocean basin	×	×	×	≃	✓	✓
Rotational feedback	×	×	×	×	✓	✓
Numerical scheme	Green's function	FCM	FDM	FDM/FCM	spherical harmonics	diverse
Computational cost	low	low	low	low	intermediate	high

Table 1. Comparison of the GIA model families available at the time of this publication.

FastIsostasy against analytical, 1D GIA and 3D GIA solutions in the results section before discussing the limitations, future improvements and novel contributions of the model.

2 Model description

M_E (kg)	r_E (km)	g (m s^{-2})	ρ^{ice} (kg m^{-3})	ρ^{sw}	ρ^{l}	ρ^{m}	E_0 (Pa)	ν_0 (1)	A^{o}_{pd} (m^2)
$5.972 \cdot 10^{24}$	6371	9.8	910	1028	3200	3400	$6.6 \cdot 10^{10}$	0.28	$3.625 \cdot 10^{14}$

Table 2. Numerical values of constants in FastIsostasy. Values for the solid Earth are largely derived from the Preliminary Reference Earth Model (PREM) (Dziewonski and Anderson, 1981) and the ocean surface from Cogley (2012).

2.1 Preliminary considerations

145 As depicted in Fig. 3, FastIsostasy assumes a rectangular domain $\Omega \subset \mathbb{R}^2$, obtained from a projection of the spherical Earth onto a Cartesian plane with dimensions $2W_x$ and $2W_y$, respectively in the directions of the lateral coordinates x and y. We

introduce the uniform spatial discretization step $h_x = h_y = h$ such that the domain is subdivided into $N_x \times N_y$ cells, with $N_x, N_y \in \mathbb{N}$. We define all variables that are not specified as scalars (c.f. Table 2) to be smooth fields, as, for instance, the vertical load $\sigma^{zz}(x, y, t) : \mathbb{R}^3 \to \mathbb{R}$. For convenience, we will omit the space and time dependence from now on. The discretized

150 equivalent of smooth fields are denoted by bold symbols, e.g. $\boldsymbol{\sigma^{zz}} \in \mathbb{R}^{N_x \times N_y}$ and their entries by the index notation $\sigma^{zz}_{i,j}$, with $i \in \{1, 2, \ldots, N_x\}$, $j \in \{1, 2, \ldots, N_y\}$. The field of vertical load is expressed as:

$$\sigma^{zz} = -g \left(\rho^{\text{ice}} \Delta H^{\text{ice}} + \rho^{\text{sw}} \Delta H^{\text{sw}} + \rho^{\text{sed}} \Delta H^{\text{sed}} \right), \tag{1}$$

with $g = 9.8 \, \text{m} \, \text{s}^{-2}$ the gravitational acceleration, ρ^{ice}, ρ^{sw} and ρ^{sed} respectively the mean densities of ice, seawater and sediment.[1] The height anomalies ΔH^{ice}, ΔH^{sw} and ΔH^{sed} of the corresponding columns are defined with respect to the initial

155 condition, assumed to represent a configuration close to equilibrium. On this domain, the first and second spatial derivatives of a placeholder field M can be computed with central differences:

$$
\left.
\begin{aligned}
\mathcal{D}_x M_{i,j} &= \frac{M_{i,j+1} - M_{i,j-1}}{2 \, h \, K_{i,j}}, & \mathcal{D}_y M_{i,j} &= \frac{M_{i+1,j} - M_{i-1,j}}{2 \, h \, K_{i,j}}, \\
\mathcal{D}_{xx} M_{i,j} &= \frac{M_{i,j-1} - 2M_{i,j} + M_{i,j+1}}{h^2 \cdot K_{i,j}^2}, & \mathcal{D}_{yy} M_{i,j} &= \frac{M_{i-1,j} - 2M_{i,j} + M_{i+1,j}}{h^2 \cdot K_{i,j}^2}, \\
\mathcal{D}_{xy} M_{i,j} &= \mathcal{D}_y \left(\mathcal{D}_x M_{i,j} \right),
\end{aligned}
\right\}
\tag{2}
$$

with K the distortion factor of the chosen projection.[2] Furthermore, the pseudo-differential operator $|\nabla|$ of a placeholder matrix $\boldsymbol{M}$ is adapted from Bueler et al. (2007) to suit non-equispaced grids:

160 $$|\nabla| \boldsymbol{M} = \mathcal{F}^{-1} \left(\boldsymbol{\kappa} \odot \mathcal{F}(\boldsymbol{M}) \right) \oslash \boldsymbol{K}, \tag{3}$$

with $\odot$ the element-wise product, $\oslash$ the element-wise division, $\mathcal{F}$ the Fourier transform, $\mathcal{F}^{-1}$ its inverse and $\boldsymbol{\kappa}$ the coefficient matrix derived in Bueler et al. (2007). Models that do not account for distortion underestimate the length and area of cells away from the reference latitude and therefore require a domain with restricted spatial extent, a limitation that is here overcome.

2.2 Lumping the depth dimension

165 As depicted in Fig. 3, the vertical structure of the solid Earth is modelled by a stack of layers along the vertical dimension z. With the layer index $l \in \{0, 1, \ldots, L-1, L\}$ going from top to bottom, the layers are:

– $l = 0$: an elastic plate with Young modulus $E_0 = \text{constant}$, Poisson ratio $\nu_0 = \text{constant}$, and laterally-variable thickness $T_0(x, y)$.

---

[1]In the present work, the contribution from sediments will be ignored but FastIsostasy's API already accepts external forcing from sediments.
[2]The distortion K does not appear in σ^{zz} since it cancels out when computing the volume-to-area ratio.
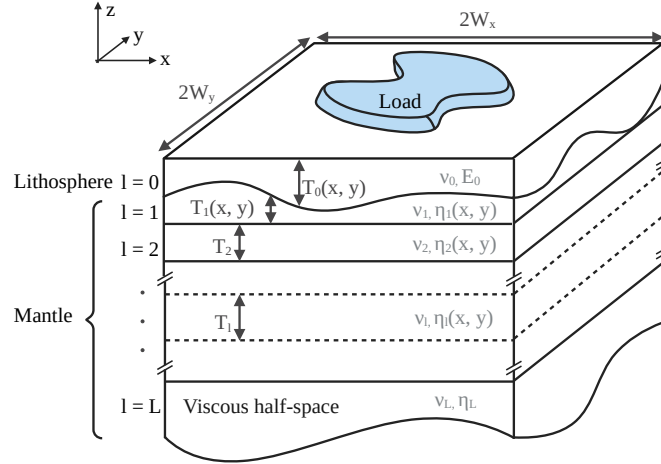
Figure 3. Schematic representation of a typical FastIsostasy domain.

- $l \in \{1, 2, \ldots, L-2, L-1\}$: an arbitrary number of viscous channels, each with Young modulus $E_l = \text{constant}$, Poisson ratio $\nu_l = \text{constant}$ and viscosity $\eta_l(x, y)$. As depicted in Fig. 3, the first of these layers has a laterally-variable thickness $T_1(x, y)$ that is complementary to $T_0(x, y)$ and allows all further layers to have a homogeneous one $T_l(x, y) = \text{constant}$ for $l \geq 2$.

- $l = L$: a viscous half-space with Young modulus $E_L = \text{constant}$, Poisson ratio $\nu_L = \text{constant}$ and homogeneous viscosity $\eta_L = \text{const}$.

Whereas $l = 0$ represents the lithosphere, all further layers represent the remaining mantle. To avoid resolving the depth-dimension, FastIsostasy lumps the latter layers into a single one by computing a so-called *effective viscosity* for the whole mantle. The key to do so is provided by Cathles (1975), where a three-layer model including an elastic plate, a viscous channel and a viscous half-space is converted into a two-layer model where the viscous channel and the viscous half-space have been lumped into a single half-space by introducing following scaling factor:

$$R(\kappa, \tilde{\eta}, T) = \frac{2\tilde{\eta} C(\kappa) S(\kappa) + \left(1 - \tilde{\eta}^2\right) T^2 \kappa^2 + \tilde{\eta}^2 S(\kappa)^2 + C(\kappa)^2}{(\tilde{\eta} + \tilde{\eta}^{-1}) C(\kappa) S(\kappa) + (\tilde{\eta} - \tilde{\eta}^{-1}) T\kappa + S(\kappa)^2 + C(\kappa)^2}, \tag{4}$$

with T the channel thickness, $\tilde{\eta}$ the channel viscosity divided by the half-space viscosity, $C(\kappa) = \cosh(T\kappa)$, $S(\kappa) = \sinh(T\kappa)$ and κ the wavenumber of the load. Hence, solving the 3-layer case can be formulated as solving the 2-layer case with the half-space viscosity scaled by R. We propose to generalise this idea by performing an induction from the bottom to the top layers, i.e., with decreasing l:

Initialisation: layer $l = L$ is a viscous half-space with $\eta_l^{\text{eff}} = \eta_L$,

Induction step: layer $l + 1$ can be represented as viscous half-space with η_{l+1}^{eff} and is overlain by a viscous channel l. These can be converted in an equivalent half-space with effective viscosity:

$$\eta_l^{\text{eff}} = R\left(\kappa, \frac{\eta_l}{\eta_{l+1}^{\text{eff}}}, T_l\right) \cdot \eta_{l+1}^{\text{eff}}. \tag{5}$$

190   Thus, η_1^{eff} is the effective viscosity of the half-space representing the compound of layers $l \in \{1, 2, \ldots, L-1, L\}$. In essence, this represents a nonlinear mean of the viscosity over depth and allows accounting for an arbitrary number of layers in a regional model. Since a load wavenumber $\kappa = \pi W^{-1}$ has to be chosen for this procedure, we here introduce a source of error compared to 1D and 3D GIA models. In the present work, we set the characteristic length W of the load to be $1000\,\text{km}$, a value suited for the computation on the scale of continental ice sheets. Finally, to account for compressibility and lateral variations

195   of the shear modulus, a scaling α of the viscosity is introduced and described in Sect. A:

$$\eta = \alpha\,\eta_1^{\text{eff}}. \tag{6}$$

This gives the corrected effective viscosity η, which brings the Maxwell time of FastIsostasy close to that of a 3D GIA model. Although converting the 3D problem into a 2D one introduces an error, it also greatly reduces the computational cost. In particular, the partial differential equation (PDE) governing an elastic plate on a viscous half-space can be transformed into an

200   ordinary differential equation (ODE), as we describe in the next section.

2.3   LV-ELVA

We now assume that the aforementioned lumping of the layers has been performed and that the lithosphere and underlying mantle are represented by an elastic plate overlaying a viscous half-space. Since the vertical extent of the plate is typically two orders of magnitude smaller than its horizontal one, it is considered to be thin. By assuming a Maxwell rheology, the vertical

205   displacement $u^{\text{tot}} = u^e + u$ of the bedrock resulting from a stress σ^{zz} can be decomposed in an elastic and a viscous response, respectively denoted by u^e and u. In its current version, FastIsostasy only computes the vertical displacement of the bedrock, since the horizontal one has a negligible impact on ice-sheet dynamics. Nonetheless, it might be used to constrain the model through GPS measurements and its implementation is left for future versions of the model.

Computing the elastic response of the lithosphere can be done by convoluting the load σ^{zz} with an appropriate Green's

210   function Γ^e:

$$u^e = \Gamma^e \otimes \frac{K^2 \sigma^{zz}}{g}. \tag{7}$$

This represents the instantaneous compression of the lithosphere and accounts for the distortion resulting from the projection. In reality, this process takes place on the time scale of days, but can be considered to be immediate compared to the long time

scales of the viscous response and the ice-sheet dynamics. To construct the elastic Green's function, tabulated values from
215 Farrell (1972) are used and show great agreement with a 3D GIA model in Test 3.

When material from the solid Earth is displaced, a hydrostatic force counteracting the load arises. We define the pressure
field p as the sum of all these effects:

$$p = \sigma^{zz} - g\left(\rho^{\mathrm{l}}\,u^{e} + \rho^{\mathrm{m}}\,u\right), \tag{8}$$

with ρ^{l} and ρ^{m} mean densities of the lithosphere and the upper mantle. Since the displacement occurs in Earth's outermost
220 layers, we here assume g to be constant over these shallow depths. 3D GIA models usually represent the elastic lithosphere as
a viscous layer with very high viscosity and the elastic displacement therefore also implies a hydrostatic force. We argue that
this is closer to reality and adapt this point of view to the present context by including the elastic displacement in Eq. 8, unlike
Bueler et al. (2007) and Coulon et al. (2021). The evolution of the viscous displacement is therefore coupled to the elastic one
and is governed by:

225 $$2\eta\,|\nabla|\left(\frac{\partial u}{\partial t}\right) = p + \frac{\partial^2 M_{xx}}{\partial x^2} + 2\frac{\partial^2 M_{xy}}{\partial x \partial y} + \frac{\partial^2 M_{yy}}{\partial y^2} = F, \tag{9}$$

with η the upper-mantle viscosity field and M_{xx}, M_{yy}, M_{xy} the flexural moments for a thin plate (Ventsel and Krauthammer,
2001; Coulon et al., 2021):

$$M_{xx} = \int_{-h/2}^{h/2} \sigma^{xx} z dz = -D\left(\frac{\partial^2 u}{\partial x^2} + \nu\frac{\partial^2 u}{\partial y^2}\right), \tag{10}$$

$$M_{yy} = \int_{-h/2}^{h/2} \sigma^{yy} z dz = -D\left(\frac{\partial^2 u}{\partial y^2} + \nu\frac{\partial^2 u}{\partial x^2}\right), \tag{11}$$

230 $$M_{xy} = \int_{-h/2}^{h/2} \sigma^{xy} z dz = -D(1-\nu)\frac{\partial^2 u}{\partial x \partial y}. \tag{12}$$

In these equations, $D = D(x,y) = E_0 T_0^3/(12(1-\nu_0^2))$ is the lithospheric rigidity field.

The PDE can be understood as a an ad-hoc generalisation of both ELVA (Cathles, 1975; Lingle and Clark, 1985; Bueler
et al., 2007) and LV-ELRA (Coulon et al., 2021). Though we did not yet manage to formally derive it by generalising the work
of Cathles (1975) to heterogeneous viscosities, setting $\eta = \eta(x,y)$ in Eq. 9 yields results that are very close to those of a 3D
235 GIA model, as shown in Sect. 4. The right-hand side F of the PDE can be evaluated by applying a finite difference method
(FDM), as defined in Eq. 2:

$$\boldsymbol{F} = \boldsymbol{p} + \mathcal{D}_{xx}\boldsymbol{M}_{xx} + 2\mathcal{D}_{xy}\boldsymbol{M}_{xy} + \mathcal{D}_{yy}\boldsymbol{M}_{yy}. \tag{13}$$

By making use of Eq. 3 and rearranging terms, the time derivative of the displacement can be computed from Eq. 9 by applying
a hybrid FCM/FDM:

$$240 \quad \frac{\partial \boldsymbol{u}}{\partial t} = \mathcal{F}^{-1}\left(\mathcal{F}(\boldsymbol{F} \odot \boldsymbol{K} \oslash 2\boldsymbol{\eta}) \oslash (\boldsymbol{\kappa} + \boldsymbol{\varepsilon})\right), \qquad (14)$$

with $\varepsilon \ll 1$ a regularisation term to avoid division by 0. Thus, without the need of solving large systems of linear equations,
we obtain an ODE that can be solved with explicit integration methods. Note that in Bueler et al. (2007) the closed form of
a Crank-Nicolson (implicit) scheme is given, thus providing unconditional stability. Due to the complexity of the right-hand
side, finding such a closed form for LV-ELVA is more challenging and goes beyond the scope of this work. We emphasise that

245 the smaller time steps resulting from explicit schemes might nevertheless be needed for (1) coupling purposes, as an iterative
scheme for convergence of the ice-sheet and solid-Earth history can be avoided, and (2) capturing with enough accuracy the
fast dynamics that can occur in regions of low viscosity.

Formally, we require the far-field displacement to be zero. However, FCM does not allow explicit treatment of such boundary
conditions (BCs). To enforce its approximate representation, we subtract the mean displacement of the corner vertices from the

250 solution at each time step, which is here expressed with the common choice of notation from programming:

$$u_{i,j}(t) := u_{i,j} - \frac{1}{4}(u_{1,1}(t) + u_{1,N_y}(t) + u_{N_x,1}(t) + u_{N_x,N_y}(t)). \qquad (15)$$

Note that this differs from Bueler et al. (2007), where the whole domain boundary is used for this purpose. We argue that our
approach is a better representation of the required BC because (1) corner points are further away from the load and (2) are
equidistant from the centre of a rectangular domain.

255 **2.4 Regional sea-level model**

Assuming a fixed ocean surface to compute the evolution of the sea level can lead to a bias of tens of metres over glacial cycles.
To tackle this, we propose an extension of Goelzer et al. (2020) that accounts for the time dependence of the ocean surface
$A^{\mathrm{o}}(t)$ when computing $s(t)$, the barystatic sea level (BSL). The volume change of the ocean at time step k is defined as:

$$V_k = V^{\mathrm{af}} \frac{\rho^{\mathrm{ice}}}{\rho^{\mathrm{sw}}} + V^{\mathrm{pov}} + V^{\mathrm{den}}, \qquad (16)$$

260 with V^{af} the contribution from ice above flotation, $\mathrm{V}^{\mathrm{pov}}$ the contribution from changes in the bedrock height and $\mathrm{V}^{\mathrm{den}}$ the
contribution from density differences between meltwater and seawater. We refer to Goelzer et al. (2020) for the detailed
computation of these quantities, which are defined with respect to a reference state, typically the present-day one.

Global GIA models typically compute the evolution of shorelines, leading to an important nonlinearity in the sea-level
equation (Mitrovica and Milne, 2003; Kendall et al., 2005). We propose to solve this nonlinear relation in a simplified way,

265 by introducing $\Delta V_k = V_k - V_{k-1}$, the volume change over a time step $\Delta t = t_k - t_{k-1}$, which in turns leads to a change

$\Delta s_k = s_k - s_{k-1}$ of the BSL. Over small time intervals $\mathcal{O}(\Delta t) = 10\,\mathrm{yr}$, the change in ocean volume is small enough to be approximated by a trapezoidal rule, depicted in Fig. 4 and leading to the following equation:

$$\Delta V_k = (s_k - s_{k-1})\frac{A^{\mathrm{o}}(s_k) + A^{\mathrm{o}}(s_{k-1})}{2}. \tag{17}$$

This equation is solved by using s_{k-1} as an initial guess and the updated BSL s_k is typically obtained after a few iterations of
270   the nonlinear solver. The function $A^{\mathrm{o}}(s) : \mathbb{R} \to \mathbb{R}$ is here computed by summing the surfaces of cells situated below the BSL, based on the 1 arc-minute global topography of ETOPO1 (Amante and Eakins, 2009). Note that this slightly overestimates the ocean surface, since all regions below sea-level are counted as part of the ocean, including, for instance, most of the Netherlands. To tackle this, we introduce a bias correction scaling γ, which avoids any offset for the present-day value $A^{\mathrm{o}}_{\mathrm{pd}}$ and depends on the uncorrected value $\tilde{A}^{\mathrm{o}}(s)$:

275   $$A^{\mathrm{o}}(s) = \gamma \tilde{A}^{\mathrm{o}}(s), \qquad \text{with}: \quad \gamma = \frac{A^{\mathrm{o}}_{\mathrm{pd}}}{\tilde{A}^{\mathrm{o}}(s=0)}. \tag{18}$$

To reduce the run time, we precompute $A^{\mathrm{o}}(s)$ as a piecewise-linear interpolator for $\mathrm{SLC} \in [-150, 70]\,\mathrm{yr}$ with a discretization of $\Delta\mathrm{SLC} = 0.1\,\mathrm{m}$. The resulting function is depicted in the bottom-left panel of Fig. 4 and shows that, for the range of realistic sea-level contributions over glacial cycles, the trapezoidal approximation leads to variations of the ocean surface between -7% and +4% around the present-day value. Although this is a rough approximation of the ocean surface evolution, it is
280   an improvement compared to fixing $A^{\mathrm{o}}(t) = A^{\mathrm{o}}_{\mathrm{pd}}$. In particular, the bottom-right panel of Fig. 4 shows that the LGM sea level is overestimated by about $5\,\mathrm{m}$ for fixed ocean boundaries compared to the trapezoidal approximation. This can lead to differences of several kilometres in the grounding line position, depending on the local bedrock slope. We emphasise that a more sophisticated approach than ours is likely to require a global domain, which we here want to avoid.

We then compute the sea-surface height perturbation N as in (Coulon et al., 2021) - that is, by convoluting the Green function
285   Γ^N of sea-surface height with the mass column anomaly:

$$N = \Gamma^N \otimes \frac{K^2 p}{g}, \qquad \text{with}: \quad \Gamma^N(\theta) = \frac{R_e}{M_e}\left(\frac{1}{2\sin(\theta/2)}\right), \tag{19}$$

R_e the Earth's radius, M_e the Earth's mass and θ the colatitude. To avoid $\theta = 0$, we impose a minimal colatitude of the order of the resolution. Finally, the regional sea-level field $\mathrm{SL}(x, y, t)$ is updated by:

$$\mathrm{SL}(x, y, t) = s(t) + N(x, y, t) + c(t), \tag{20}$$

290   In a global model, $c(t)$ is a scalar ensuring conservation of mass, which is however impossible to impose on a regional model with open boundaries. In contrast, we here use $c(t)$ to impose a zero sea-surface height perturbation in the far field, similar to Eq. 15. Note that we apply this BC on the extended domain, on which the result of a convolution is typically computed.
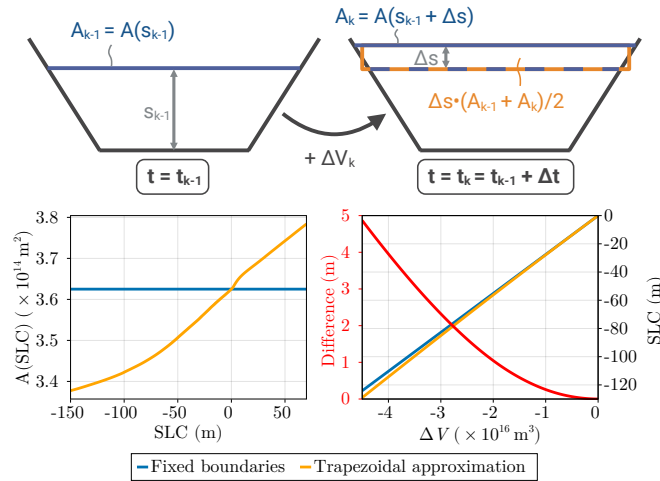
Figure 4. (Top) Schematic representation of the trapezoidal approximation used to solve the nonlinearity of the sea-level equation. (Bottom left) Ocean surface over barystatic change of sea level with respect to present day, for fixed boundaries versus the trapezoidal approximation of the basin evolution. (Bottom right) Sea level computed for a change in ice volume equivalent to LGM, for fixed boundaries versus the trapezoidal approximation.

Furthermore, we draw attention upon the fact that Eq. 20 implies that the load at the domain boundary can change over time. This is however incompatible with the treatment of the BCs outlined in Eq. 15 and we therefore impose the load anomaly to

295   be zero outside of a predefined mask. This mask is typically larger than the LGM extent of the ice sheet and thus prevents us from ignoring important changes in the load, while avoiding deformation in the far field that cannot be handled with an FCM. We call this adaptation of previous work (Goelzer et al., 2020; Coulon et al., 2021) the Regional Sea-Level Model (ReSeLeM). FastIsostasy is, in essence, a coupling between LV-ELVA and ReSeLeM.

3   Implementation, performance and further remarks

300   FastIsostasy has been implemented in Julia (FastIsostasy.jl) and in Fortran. Julia (Bezanson et al., 2017) is a high-performance language with a vast ecosystem, on which FastIsostasy.jl relies to offer convenient features and good performance:

1. To evaluate the right-hand side of the ODE obtained in Eq. 14 and perform the convolutions used to compute the elastic and the sea-surface response, FastIsostasy.jl relies on forward and inverse Fast-Fourier Transforms (FFTs), which are implemented in an optimised way in FFTW.jl (Frigo and Johnson, 2005). Evaluating the right-hand side therefore

305   displays a computational complexity of $\mathcal{O}\left(N \log_2 N\right)$, for a matrix of size $N = N_x \times N_y$. To achieve an even better speed increase, (1) N_x, N_y are generally chosen as powers of 2, (2) FFT plans are pre-computed during the initialisation of the computation domain and (3) the transforms are computed in-place to reduce the memory allocation.

2. To subsequently integrate the right-hand side in time, FastIsostasy.jl relies on OrdinaryDiffEq.jl (Rackauckas and Nie, 2017), a package that offers a wide range of optimised routines. We here restrict ourselves to explicit methods, which however range from the simplest explicit Euler up to schemes of order 14. Explicit time-integration schemes typically require decreasing the time step with increasing spatial resolution to prevent instabilities. This requires more evaluations of the right-hand side and leads the scaling of computational complexity for the full problem to be higher than $\mathcal{O}(N \log_2 N)$. In FastIsostasy.jl, stability is enforced at minimal cost by relying on the adaptive time-stepping methods of OrdinaryDiffEq.jl. By providing keyword arguments, the user is able to influence any option related to the time integration, such as the scheme, the error tolerance, the minimal time-step, etc.

3. FastIsostasy.jl relies on CUDA.jl (Besard et al., 2019b, a) and ParallelStencil.jl to optionally run performance-relevant computations on a GPU (so far restricted to NVIDIA hardware). Due to their heavily parallelised architecture, GPUs are able to scale better than CPUs for some computations - in our case, the FFT-related operations mentioned above. The speed increase thus obtained will be illustrated in Test 1 of the model validation. Offering a GPU-parallelised GIA code is unprecedented to our knowledge and only requires the user to set the keyword argument `use_cuda=true`.

4. In FastIsostasy.jl, the nonlinearity introduced by the time-dependent ocean surface is solved by using NLsolve.jl, in combination with an interpolator of $A(\text{SLC})$, which is constructed at initialisation using Interpolations.jl. Since $A(\text{SLC})$ is monotonic and initial guesses are close to the solution, the computation time associated with this step is negligible. Furthermore, whereas the adaptive time-stepping is convenient to enforce stability of the viscous displacement, updating the diagnostics - such as the elastic displacement, the ocean surface and sea level - can be done less frequently. For instance $\Delta t_{\text{diag}} = 10 \, \text{yr}$ is used in the present work and can be determined by the user through a keyword argument.

As illustrated above, FastIsostasy.jl relies on numerous Julia packages. Since it is a registered package, it can be easily installed, along all its dependencies, by simply running `add FastIsostasy` in Julia's package manager. Furthermore, it is thoroughly documented at https://janjereczek.github.io/FastIsostasy.jl/dev/, including an API reference, a tutorial and a few examples. Additionally, FastIsostasy.jl is designed in a modular way that facilitates its coupling to an ice-sheet model and we therefore believe that the implementation burden associated with its use is very low.

Since Julia does not yet support compilation to binaries, FastIsostasy is additionally programmed in Fortran to allow for compatibility with most existing ice-sheet models. Nonetheless, Fortran does not provide packages that allow convenience at the level of the Julia ecosystem. Thus, the Fortran version (1) does not allow computation on GPU, (2) only provides explicit Euler and Runge-Kutta methods of 4th order for integration in time and (3) does not allow for time-evolving ocean boundaries.

4 Model validation and benchmarks

We now validate FastIsostasy with series of tests:

– Test 1: a comparison to an analytical solution for an idealised load on a homogeneous, flat Earth. This aims to check that the numerics are well-implemented for the simplest case and that our results are comparable to Bueler et al. (2007).

340   – Test 2: a comparison to benchmark solutions of three different 1D GIA models, showing great agreement among each other. This aims to understand the discrepancies which can arise from the flat-Earth simplification and the lumping of depth-dependent viscosity profiles into a single value.

   – Test 3: a comparison to Seakon (Latychev et al., 2005; Gomez et al., 2018), a 3D GIA model, on idealised cases of LV. This aims to check whether Eq. 9 and its discretization, Eq. 14, are valid for heterogeneous parameter fields. Here we

345   will also compare the elastic displacement of Seakon versus FastIsostasy.

   – Test 4: a comparison to Seakon with realistic LV and forced by a full glacial cycle as ice history. This aims to check whether loads and Earth structures of typical applications can be reasonably well represented.

These tests are summarised in Table 3 and aim to quantify, as orthogonally as possible, each source of difference between FastIsostasy and the reference solutions listed above. This is measured by an absolute and a relative value, respectively defined

350 as:

$$
\begin{aligned}
e^{\mathrm{abs}}(x,y,t) &= |u_{\mathrm{FI}}(x,y,t) - u_{\mathrm{ref}}(x,y,t)|, & (21)\\
e(x,y,t) &= \frac{e^{\mathrm{abs}}(x,y,t)}{\max\limits_{x,y,t} |u_{\mathrm{ref}}(x,y,t)|}, & (22)
\end{aligned}
$$

with the indices "FI" and "ref" respectively indicating the FastIsostasy and reference solutions. For Test 1, we require the relative error to be at the level of only a few percent, since the problem solved by FastIsostasy is equivalent to the reference.

355 For all other tests, the reference is given by results from 1D and 3D GIA models, which intrinsically differ from FastIsostasy by relying on a global domain and by resolving the depth dimension. For these examples, larger errors are therefore to be expected and we define an acceptable upper bound of 5 and 20% for the mean and maximum relative difference respectively. This choice is motivated by the fact that, despite great efforts to improve the constraints on the upper-mantle viscosity, this quantity remains largely uncertain (Ivins et al., 2022). It is therefore easy to imagine that two simulations performed with the

360 same 3D GIA model and realistic but differently inferred viscosity fields, might display mean and maximum relative differences of up to 5 and 20% respectively. In other words, throughout the tests, the model uncertainties of FastIsostasy are required to be comparable to the parametric uncertainties inherent to any GIA model.

Test	Compared to...	Load	T, η	L
1	Analytical solution	Ice cylinder	homogeneous	2
2	1D GIA models	Ice cylinder & ice cap	homogeneous	3
3	3D GIA model	Ice cylinder	Gaussian heterogeneity (see Fig. A1)	3
4	3D GIA model	Glacial cycle (ICE6G)	Estimation for Antarctica (Pan et al., 2022)	4

Table 3. Summary of the tests performed using FastIsostasy.

4.1 Test 1 – Analytical solution for idealised load on homogeneous Earth

We first reproduce the test proposed in Bueler et al. (2007) by using a 2-layer model with $W_x = W_y = 3000\,\mathrm{km}$, $N = N_x =$
$N_y = 256$ and $h \simeq 23\,\mathrm{km}$. The lithosphere has a thickness $T(x, y) = 88\,\mathrm{km}$ and a viscosity $\eta(x, y) = 10^{21}\,\mathrm{Pa\,s}$. The load,
placed at the centre of the computation domain, is a flat cylinder of ice with radius $R = 1000\,\mathrm{km}$ and thickness $H = 1\,\mathrm{km}$. For
this idealised case, an analytical solution of the viscous solution is provided in Bueler et al. (2007), yielding:

$$u(r,t) = \rho^{\mathrm{ice}} g H R \cdot \int_0^\infty \beta^{-1} \left[\exp\left(-\frac{\beta t}{2\eta\kappa} \right) - 1 \right] J_1(\kappa R_0) J_0(\kappa r) \mathrm{d}\kappa, \tag{23}$$

with J_0 and J_1 the Bessel functions of first kind and respectively of order 0 and 1, and $\beta = \beta(\kappa) = \rho^{\mathrm{m}} g + D\kappa^4$. Panel (a) of
Fig. 5 shows cross-sections of the domain along the x dimension, demonstrating that the numerical solution closely follows
the analytical one. In complement, panel (b) shows the corresponding maximal and mean error over time. It appears that
for $t \geq 5000\,\mathrm{yr}$, the viscous displacement is captured with $\mathrm{mean}(e^{\mathrm{abs}}) < \max(e^{\mathrm{abs}}) < 1\,\mathrm{m}$. For $t \leq 2000\,\mathrm{yr}$, the displacement
surface is well captured in terms of shape but appears to be slightly shifted along the z-dimension, due to the approximate
treatment of the BCs as written in Eq. 15 and leading to an error of up to $e^{\mathrm{abs}} \simeq 5\,\mathrm{m}$, which corresponds to $e \simeq 0.02$. Whereas
in Bueler et al. (2007) a correction of this effect is applied based on the knowledge of the analytical solution, we here decide
not to do so. First, because such correction only applies to this specific case and second, because users should be informed
about the upper bound of numerical error that will arise in their own experiments. In fact, for this idealised case, the forcing is
a step function in time, thus leading to unrealistically high rates of ice volume change. This in turns leads to errors resulting
from Eq. 15 that are larger than for realistic applications, where the load is coherent in space and time.

Panel (c) shows that the maximal and mean equilibrium error respectively decrease with $\mathcal{O}(-0.4)$ and $\mathcal{O}(-0.36)$ in $\log_2 - \log_{10}$
space, showing that convergence to the analytical solution of equilibrium can be achieved relatively quickly with increasing
resolution. To study the run-time on CPU (Intel i7-10750H 2.60GHz) versus GPU (NVIDIA GeForce RTX 2070), the computa-
tions of Test 1 have been performed with an explicit Euler scheme with fixed time step. This isolates the evaluated computation
time from the influence of adaptive time-stepping. The results are depicted in panel (d) and show that using a GPU is advan-
tageous for $N \geq 128$, which corresponds to the typical problem size for ice-sheet modelling. More specifically, the CPU and
GPU computation time respectively increase with $\mathcal{O}(0.6)$ and $\mathcal{O}(0.02)$ in $\log_2 - \log_{10}$ space, thus giving a clear advantage to
GPU computation for large problems. Thanks to the hybrid FCM/FDM scheme used to evaluate Eq. 14, the scaling of compu-
tation time on both CPU and GPU is better than is usually obtained from finite difference, volume or element methods, since
all of them rely on the expensive operation of solving a large system of linear equations.

4.2 Test 2 – 1D GIA solutions of idealised loads on layered Earth

In Spada et al. (2011), a range of 1D GIA models are benchmarked against each other and show great agreement on various
experiments. Here, we reproduce the benchmark tests called "1/2" (geodetic quantities) and "2/2" (geodetic rates), which are
similar to Test 1 but presents following differences:
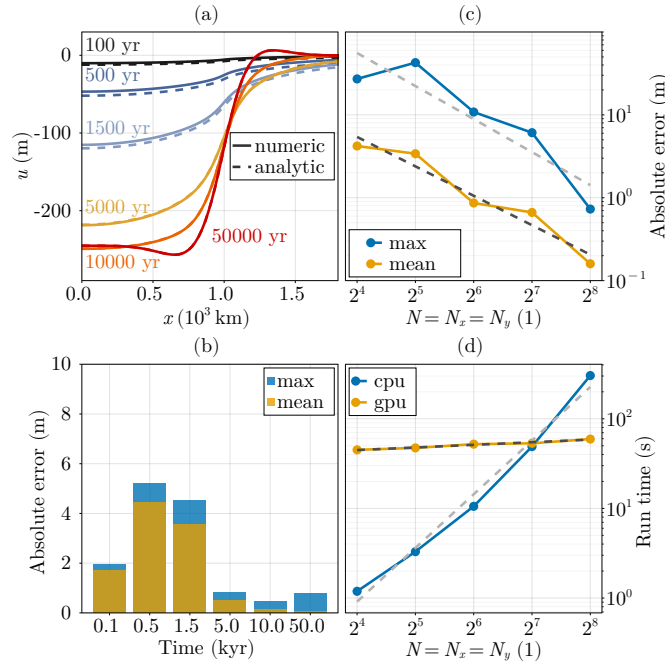
Figure 5. (a) Transient cross-sections of bedrock displacement along x-axis, from the center of the domain until $x = 1800$ km. The resolution used here is $N_x = N_y = 2^8$, $h \simeq 23$ km. (b) Corresponding mean and maximal errors over time. (c) Resolution-dependence of maximum and mean error at equilibrium with respect to the analytical solution, with the light and dark gray dashed lines, respectively, corresponding to $\mathcal{O}(-0.4)$, $\mathcal{O}(-0.36)$ in $\log_2 - \log_{10}$ space. (d) Resolution dependence of the computation time on CPU versus GPU, with the light and dark gray dashed lines respectively corresponding to $\mathcal{O}(0.6)$, $\mathcal{O}(0.02)$ in $\log_2 - \log_{10}$ space.

    – The computation domain is a spherical Earth on which we apply ice loads with $\rho^{\mathrm{ice}} = 931 \, \mathrm{kg \, m^{-3}}$, chosen in agreement

395   with Spada et al. (2011), and following geometries:

    (A) a cylindrical ice load of thickness $H = 1$ km and radius $\theta = 10°$,

    (B) an ice cap with maximal height $H_{\mathrm{max}} = 1.5$ km, radius $\theta = 10°$ and its shape defined by a cosine function.

    – The Earth structure has three layers, namely (1) a lithosphere of thickness $T_0 = 70$ km and shear modulus $G_0 = 5 \cdot$

400   10^{11} Pa, (2) an upper mantle of thickness $T_1 = 600$ km and viscosity $\eta_1 = 10^{21}$ Pa s and (3) a lower mantle reaching down to the core-mantle boundary with a viscosity $\eta_2 = 2 \cdot 10^{21}$ Pa s. For any further detail, we refer to the M3-L70-V01 profile shown in (Spada et al., 2011). In FastIsostasy, these layers are translated into a quasi-elastic plate, a viscous channel and a viscous half-space.

    – The sea-surface height results provided in Spada et al. (2011) allow us to check the validity of Eq. 19, used in FastIsostasy.
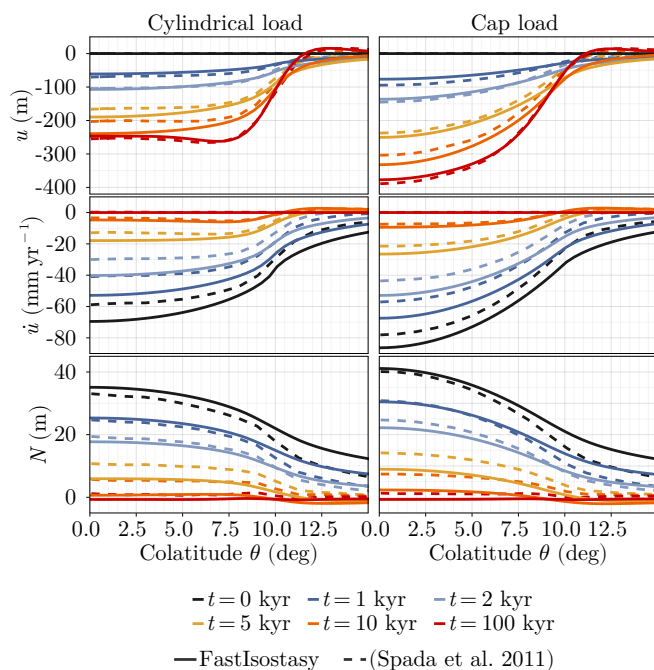
Figure 6. Comparison of FastIsostasy versus Spada et al. (2011) on tests "1/2" and "2/2". From top to bottom: viscous displacement u, viscous displacement rate $\dot{u}$ and resulting sea-surface height perturbation N. From left to right: cylinder and cap of ice applied as load.

It appears in Fig. 6 that the viscous displacement, its rate and the sea-surface height computed in FastIsostasy reasonably follow the results of Spada et al. (2011). The latter corresponds to the outputs of PMTF, VILMA (Martinec, 2000) and VEENT which show such good agreement that they are lumped into a single output. The maximal difference of u between FastIsostasy and Spada et al. (2011) arises for the cylindrical load and yields $e^{\mathrm{abs}} < 40\,\mathrm{m}$, i.e. $e < 0.16$. In contrast, the cap load leads to maximal value of $e^{\mathrm{abs}} < 30\,\mathrm{m}$, i.e. $e < 0.07$. In both cases, the difference in vertical displacement propagates to the computation of the sea-surface height according to Eq. 8 and Eq. 19. The relative maximal difference in sea-surface height between FastIsostasy and the 1D GIA models thus yields a similar value, reaching at most 15% of the maximal sea-surface height displacement.

Since the experimental setup is strictly the same for the 1D GIA models and FastIsostasy, the differences in viscous displacement can be largely attributed to the lumping of the depth dimension, which leads the two approaches solving different equations. Given the relatively small maximal differences, FastIsostasy can be used to replace a 1D GIA model for regional ice-sheet modelling since it reduces the computation time while allowing excellent resolution in time, thus avoiding sophisticated schemes for coupling to the ice-sheet model. This represents a significant improvement relative to the results presented by ELRA in Konrad et al. (2014).

4.3   Test 3 – 3D GIA solution of idealised load on idealised LV-Earth

Seakon is a 3D GIA model (Latychev et al., 2005; Gomez et al., 2018) that has been extensively used in GIA studies (e.g.
Mitrovica et al., 2009; Austermann et al., 2021; Pan et al., 2021, 2022) and even coupled to an ice-sheet model in (Gomez
et al., 2018). We here propose to benchmark FastIsostasy against Seakon on idealised cases with LV similar to that estimated
across Antarctica. Here again, a cylindrical ice load with $H = 1\,\mathrm{km}$ and $R = 1000\,\mathrm{km}$ is applied upon a domain with $W_x =$
$W_y = 3000\,\mathrm{km}$ and only two layers: the lithosphere and the mantle. We distinguish four cases (a-d) which are all parametrised
by a Gaussian-shaped anomaly that is almost zero on the boundary and yields its largest value at the interior of the domain.
For case A (case B), this anomaly represents a decrease (increase) from $T = 150\,\mathrm{km}$ down to $T = 50\,\mathrm{km}$ (up to $T = 250\,\mathrm{km}$)
of the lithspheric thickness towards the interior of the domain. For case C (case D), this anomaly represents a logarithmic
decrease (increase) from $\eta = 10^{21}\,\mathrm{Pa\,s}$ down to $\eta = 10^{20}\,\mathrm{Pa\,s}$ (up to $\eta = 10^{22}\,\mathrm{Pa\,s}$) of the mantle viscosity towards the interior
of the domain. The heterogeneities (a-d) are represented in Fig. A1 and are used to generate results that will be referred to as
FastIsostasy 3D (FI3D), since the parameter fields are dependent on x, y and z. To quantify the improvement resulting from
the use of LV-ELVA instead of ELVA, we also generate results with the nominal, homogeneous parameters $T(x, y) = 150\,\mathrm{km}$
and $\eta(x, y) = 10^{21}\,\mathrm{Pa\,s}$ and refer to this run as FastIsostasy 1D (FI1D). Furthermore, we introduce the index SK to refer to the
output of Seakon.

As can be seen in the top row of Fig. 7, FI3D closely follows Seakon on cases (a-d) by showing similar time scales,
amplitudes and shapes of the bedrock displacement. In the bottom row of Fig. 7, it appears that the maximal and mean relative
differences respectively remain at $\max(e) < 0.08$ and $\mathrm{mean}(e) < 0.04$ over time, thus satisfying the above-defined upper
bound of relative difference. We emphasise that, in an ice-sheet coupled context, looking at maximal values is more meaningful,
since the behaviour of a small region (e.g. Thwaites glacier) can lead to larger-scale impacts (e.g. the collapse of the WAIS).
Since, in the present case, even maximal differences are in a reasonable range, we argue that FastIsostasy can be used instead of
a much more expensive 3D GIA model for regional ice-sheet modelling. Despite this, it should be pointed out that FastIsostasy
systematically underestimates the peripheral forebulge by about $[10, 15]\,\mathrm{m}$. Since the latter forms in the vicinity of the ice
margin, it might be an important difference to keep in mind when comparing FastIsostasy to a 3D GIA model in a coupled
ice-sheet context.

In comparison, the differences of FI1D to Seakon are similar to those of FI3D for case (a) and only slightly higher in case
(b), with values of $\max(e) < 0.12$ and $\mathrm{mean}(e) < 0.05$. This is due to the fact that the lithospheric thickness is an important
control of the shape of the bedrock displacement but not directly of its magnitude nor time scale. This can be seen in Eq. 9,
where the lithospheric rigidity D is only multiplied with spatial derivatives of the displacement. Its impact on the displacement
magnitude can however become important when the lithosphere is thin and the load localised, since the low flexural moments
effectively decouple neighbouring cells, as displayed in Fig. A2 for the extreme case where there is no lithosphere. Furthermore,
accounting for a heterogeneous lithospheric thickness can impact the bedrock slopes significantly, which are an important
control of ice-sheet grounding-line stability and therefore of the evolution of ice sheets.
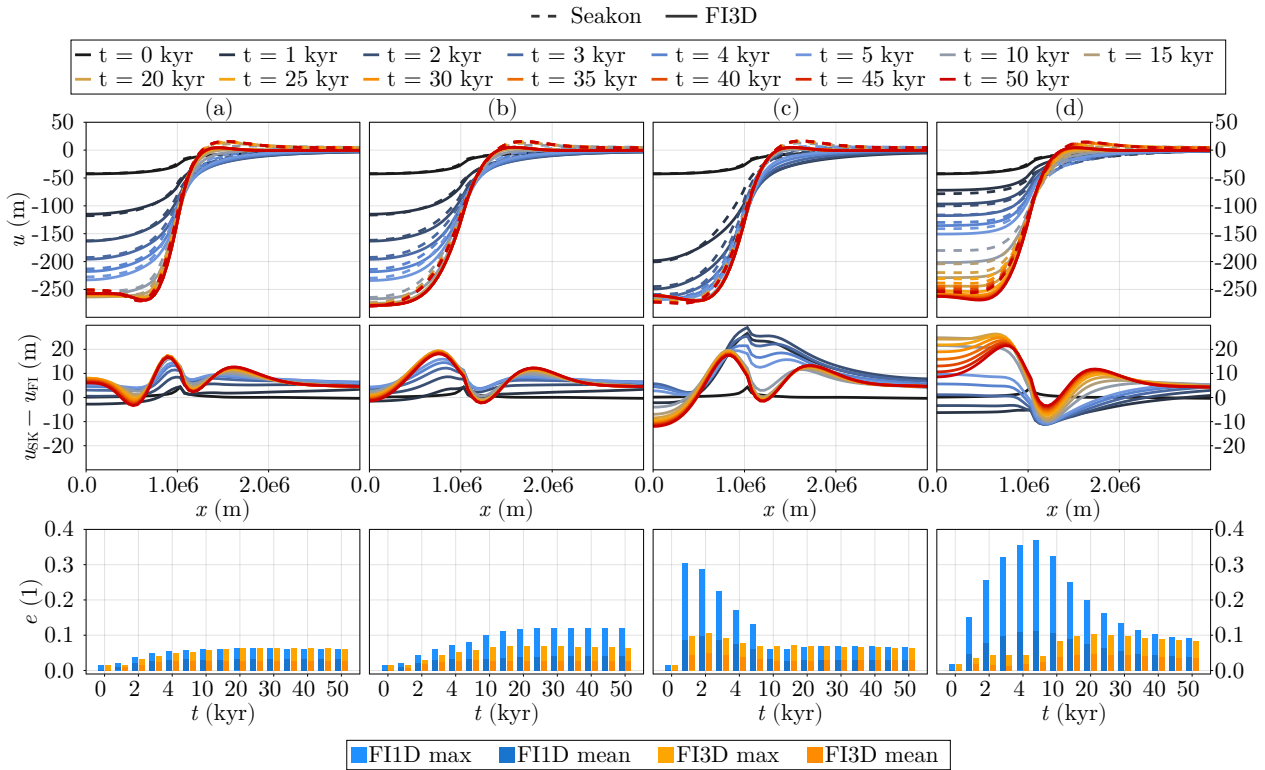
Figure 7. Comparison of FastIsostasy and Seakon for heterogeneous lithospheric thickness (a-b) and upper-mantle viscosity (c-d). (Top row) cross section of the domain along the x dimension, displaying the displacement of both models and (middle row) the corresponding difference. (Bottom row) Transient evolution of the mean and maximal relative differences of FI1D and FI3D compared to Seakon.

The advantage of using LV-ELVA over ELVA becomes more prominent when studying (c-d). For these cases, FI1D yields large transient differences compared to Seakon, reaching $\max(e) < 0.37$ and $\mathrm{mean}(e) < 0.11$. This clearly shows that ELVA, and thus ELRA, are not suited to represent the typical variations of viscosity over Antarctica and that LV-ELVA should be systematically preferred - particularly because it only requires a negligible increase of the computational cost. We stress that

455 the higher transient error of FI1D can be easily missed when considering equilibrium states, since its steady-state error is comparable to FI3D in the case of a heterogeneous lithosphere and even strictly the same in the case of a homogeneous one. Therefore, comparing models by looking at quasi-equilibrated states may be misleading. This is the case in Le Meur and Huybrechts (1996), where ELRA is validated on the final uplift map of a deglaciation - a result that ignores transient errors, which can be critical for the ice-sheet evolution.

460 We also note here that our experience has shown that a large lithospheric thickness or a low viscosity leads to the requirement of a stricter error tolerance for the adaptive time stepping. This is consistent with theoretical insights, predicting that systems

that are stiffer or that display a lower Maxwell time require smaller time steps. Most importantly, it appears through this example that Eq. 9 is capable of representing the bedrock displacement, even for significant LVs.

4.4 Test 4 – 3D GIA of the last glacial cycle on a realistic Earth

465 So far, the model has been tested with idealised loads and parameter fields. We now consider the more realistic case of simulating the GIA response of two different Earth structures to the last glacial cycle, as reconstructed in ICE6G_D (Peltier et al., 2018), an updated version of ICE6G_C (Peltier et al., 2015; Argus et al., 2014) after a mismatch with the present-day uplift was pointed out in Purcell et al. (2016). The first structure is a 1D Earth that does not present any LV. The second structure is a 3D Earth with the lithospheric thickness depicted in Fig. 2 and the mantle viscosity fields from (Pan et al., 2022), which are

470 similar to those of (Ivins et al., 2022). Combining these two structures with the two models available, we obtain a total of 4 results: Seakon 1D (SK1D), Seakon 3D (SK3D), FastIsosasy 1D (FI1D) and FastIsostasy 3D (FI3D). For FI3D, we define the depth of the model's mantle to be $300\,\mathrm{km}$, since it was observed that shallower models lead to better results. This appears plausible, since, according to Eq. 4, deeper models might overestimate the influence of deeper layers of the mantle to the effective viscosity. In Fig. A3, we provide a comparison to SK1D, confirming that FI1D can be used to mimic a 1D GIA model setting.

475 In the present section we however focus on comparing results to SK3D.

Panel (a) of Fig. 8 depicts, for all time steps, the displacement of SK3D, considered to be closest to reality, against the other results, indexed with $\{\mathrm{FI1D}, \mathrm{SK1D}, \mathrm{FI3D}\}$. We hereby only represent the points within a mask, represented by the black contours of panels (c-h) and corresponding to the LGM extent of the AIS, since this is the region of interest in ice-sheet modelling. The position around the identity shows that FI1D leads to displacements that are biased towards lower values,

480 especially for $u_{\mathrm{SK3D}} \leq -300\,\mathrm{m}$ where the error comes close to $e^{\mathrm{abs}} \simeq 130\,\mathrm{m}$. Although this bias is somewhat smaller for SK1D, it still reaches similar maximal values. In comparison, FI3D is centred around the identity and presents no such bias. This can be explained by the fact that a thinner lithosphere and a less viscous mantle in West-Antarctica allows for larger transient displacements around LGM. Furthermore, the spread around identity is an additional metric to take into account. For $u_{\mathrm{SK3D}} \geq -300\,\mathrm{m}$, SK1D, F3D and F1D respectively present the smallest, the intermediate and the largest spread.

485 Panel (b) depicts the evolution of the mean and maximal relative difference e for FI1D, F3D and SK1D with respect to SK3D. The mean and maximal value respectively relate to the spread around identity and the bias observed in panel (a). Interestingly, the peak values of $\max(e_{\mathrm{SK1D}})$ and $\max(e_{\mathrm{FI1D}})$ are very close to each other and yield about 0.22, corresponding to $\max(e^{\mathrm{abs}}) \simeq 130\,\mathrm{m}$. In both cases, these values are observed over $t \in [-22, -12]\,\mathrm{kyr}$, which correspond to the $10\,\mathrm{kyr}$ of deglaciation following LGM. This points out that high errors of FI1D and SK1D are to be expected when rapid changes of ice

490 thickness occur - a situation that could be triggered by anthropogenic climate warming. For FI1D, the peak difference to SK3D is observed at $t = -18\,\mathrm{kyr}$. The corresponding displacement fields and their difference are plotted in (c-d), corroborating that a 1D Earth structure used in FastIsostasy does not allow enough displacement in West-Antarctica after LGM. In contrast to the maximal values, the mean differences of FI1D and SK1D with respect to SK3D respectively remain below 5% and 1% at all time. This can be explained by the fact that most of the regions, especially the bulk of East Antarctica, can be well represented

495 by an intermediate mantle viscosity and lithospheric thickness. Nonetheless, the WAIS is strongly dependent on small changes
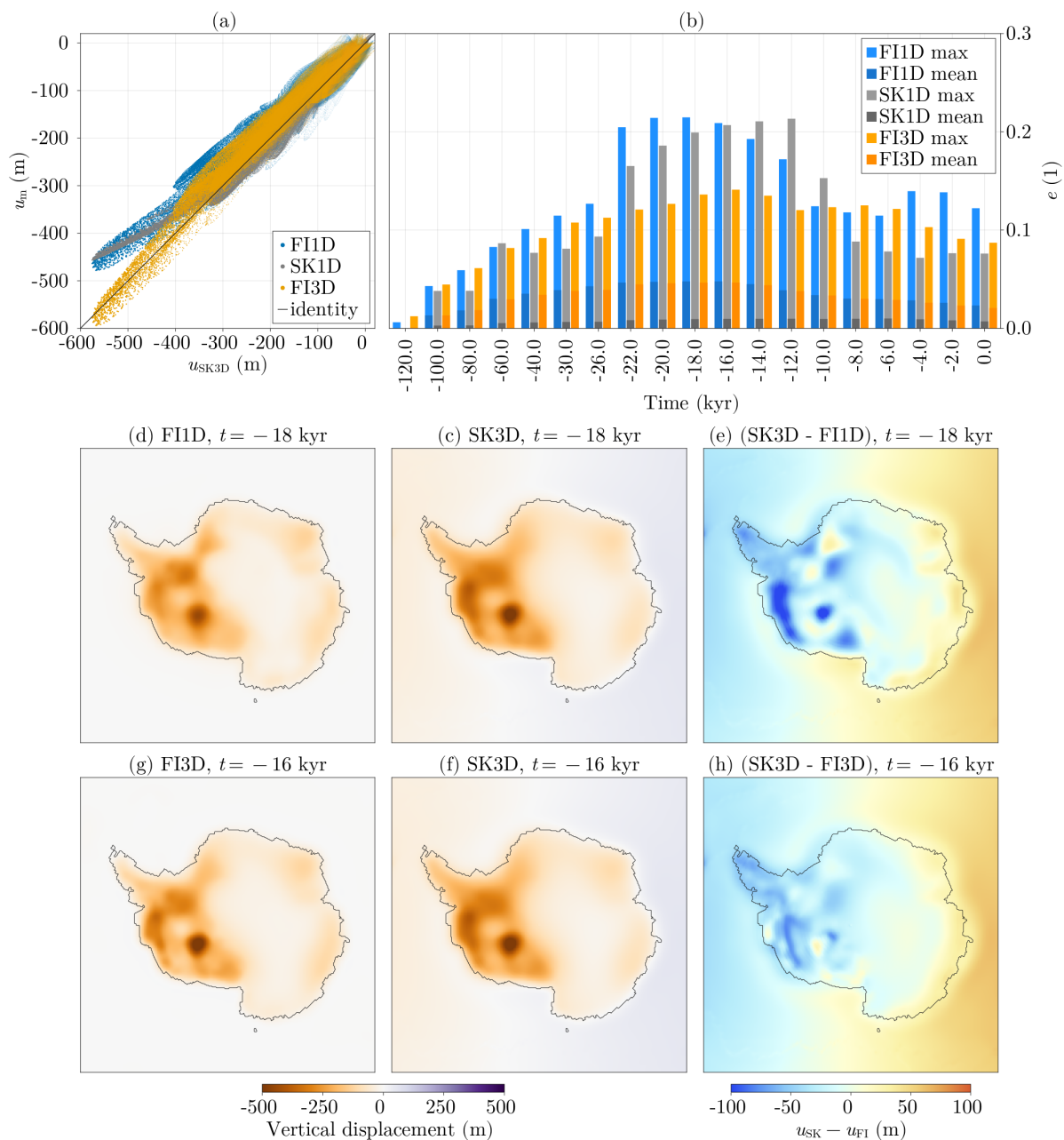
Figure 8. Comparison of Seakon and FastIsostasy, following glacial cycle loading from ICE6G_D. (a) Displacements at all time steps of u_{SK3D} versus u_{FI1D}, u_{SK1D} and u_{FI3D} for cells that are ice-covered at LGM, visualised by the black contour in panels (c-h). (b) Mean and maximal errors of u_{FI1D}, u_{SK1D} and u_{FI3D} with respect to u_{SK3D} over time. (c-e) Displacement of FI1D, SK3D and their differences for the time step of maximal error. (f-h) Displacement fields of FI3D, SK3D and their difference for the time step of maximal error.

of the grounding-line position, typically occurring in regions of lower viscosities. Therefore, large localised errors of the GIA response can have significant impacts on the evolution of the AIS and a limited amount of outliers can be arguably preferred over a slightly reduced mean error.

Compared to FI1D and SK1D, FI3D reduces the maximal error down to about $\max(e_{\text{FI3D}}) \leq 0.14$, which corresponds to $\max(e^{\text{abs}}) \leq 80\,\text{m}$ and satisfies our bound on the relative difference. The displacement fields for the time step of peak maximal error $t = -14\,\text{kyr}$ are plotted in panels (f-h) and show that the overall displacement is reasonably well matched, even in the worst case. In the near field, FI3D slightly underestimates the displacement compared to SK3D. Since this appears to be a systematic offset, it could easily be corrected by tuning the density and/or the viscosity chosen for FI3D. We however decide not to do so and give the user an idea of the differences to SK3D without additional tuning.

In (c-h), it appears that SK3D displays a subtle dipole separated by a great circle whereas FI1D and FI3D do not. By looking at the global results of SK3D, this is in fact a quadrupole and is the typical fingerprint of the rotational feedback, which is not included in FastIsostasy. This translates into a systematic albeit small error of the far field. SK1D displays the same feature and is therefore better-suited to represent the far-field displacement. Nonetheless, we stress that ice-sheet modelling requires a good representation of the near-field, which seems to be better captured by FI3D.

Despite these differences to Seakon, and potentially to any 3D GIA model, we believe that FastIsostasy can be a particularly appealing tool, since the 120 kyr run of FI3D takes only about 14 minutes to compute for a horizontal resolution of $h = 20\,\text{km}$, resulting in 350×350 grid points. For FI1D, the absence of LV leads to a reduced computation time of only about 4 minutes. These computations were performed on an NVIDIA GeForce RTX 2070, an intermediate-performance and easily accessible GPU by the standards of 2023. Although the time stepping is adaptive, no values beyond $\Delta t = 10\,\text{yr}$ are used. This contrasts with coupled studies (Gomez et al., 2018; Van Calcar et al., 2023), where the time steps are typically of the order of centuries and therefore require a coupling scheme that ensures the convergence of the ice-sheet and GIA model histories.

In comparison, the Seakon simulation takes about 4.5 days on 150 CPUs with a time step of $\Delta t \in [125, 1000]\,\text{yr}$. Assuming an ideal parallelization scaling of 100%, this corresponds to about a million minutes of CPU-runtime, or $\sim 70,000$ times more than what FastIsostasy requires. Of course, the two are not directly comparable: Seakon solves the global GIA problem, which requires many more grid points and the representation of additional processes. Seakon's output is much richer, since it includes, for instance, the position of the shorelines, the horizontal displacement of the bedrock and the relative sea level at any point on Earth. Nonetheless, these quantities tend to be irrelevant for ice-sheet modelling purposes and FastIsostasy therefore offers an opportunity to regionally mimic the behaviour of a 3D GIA model at very low computational cost.

5 Conclusions

LV-ELVA presents limitations, since it relies on a linear PDE describing the macroscopic behaviour of the solid Earth as a Maxwell body. Therefore it does not account for nonlinearities (Gasperini et al., 2004), transient rheologies (Ivins et al., 2021), composite rheologies (van der Wal et al., 2010, 2015), anisotropy (Beghein et al., 2006; Accardo et al., 2014), or microscale properties of the material (Van Calcar et al., 2023). LV-ELVA only computes the vertical displacement of the GIA and neglects

the horizontal components. Its underlying PDE was postulated here in an ad-hoc way and the regional nature of its domain
530 makes it inherently complicated to ensure conservation of mass. Furthermore, FastIsostasy does not account for Earth's rotation
and does not aim to provide global solutions, the latter being rather irrelevant since most on-going ice-sheet modelling studies
are still performed on regional domains. Future releases of FastIsostasy will focus on addressing some of these problems.

Despite the aforementioned limitations, FastIsostasy can greatly reduce the transient error of bedrock displacement compared
to ELRA, ELVA and, in some cases, even 1D GIA models, by dealing with laterally-variable Earth structures. Whereas the
535 differences between FastIsostasy and global GIA models are within the range of parametric uncertainties, the computation
time is typically reduced by 3 to 5 orders of magnitude. For most ice-sheet models, FastIsostasy thus represents a leap in GIA
comprehensiveness at very low computational cost, even for high-resolution runs on the time scale of glacial cycles. Since
fields of the lithospheric thickness and the upper-mantle viscosity can be easily found in literature, the difficulty of creating
meaningful ensembles is reduced, for instance compared with models that are not directly parametrised by the viscosity (Coulon
540 et al., 2021). The very short runtime of FastIsostasy offers an efficient method of propagating the uncertainties of the solid-Earth
parameters to future sea-level projections, thus allowing more comprehensive forecasts. Most importantly, it minimises the
misrepresentation of the GIA feedbacks in a coupled ice-sheet setting, which is particularly relevant for marine-based regions
such as the WAIS, which are likely to be the largest contributors to sea-level rise over the coming centuries. FastIsostasy is
therefore not only a convenient tool but also a reliable way to reduce biases in sea-level projections, as well as in paleoclimatic
545 simulations, for instance of glacial cycles.

We believe that even the few ice-sheet models that are coupled to a 3D GIA model can still benefit from FastIsostasy, since it
can be used as a fast-prototyping tool. In particular, a scheme to tune the parameters of FastIsostasy can turn it into an emulator
of a 3D GIA model - however with a better interpretability than, for instance, machine learning techniques. Finally, we believe
that its relatively abbreviated code and few equations compared to 1D or 3D GIA models can be suited for educational purposes.

550 *Code and data availability.* FastIsostasy.jl is available under MIT licence at https://github.com/JanJereczek/FastIsostasy.jl and the data used
in the present work can be found at https://github.com/JanJereczek/IsostasyData. The Fortran version is still work in progress. It is imple-
mented within a repository that gathers various regional models of GIA and that can be found at https://github.com/palma-ice/isostasy.

Video supplement. An animation of the thickness anomaly of ICE6G_D and the resulting bedrock displacement computed by FastIsostasy
can be found at https://github.com/JanJereczek/FastIsostasy.jl.

555 **Appendix A: Scaling the effective viscosity**

Two important characteristics of the mantle have to be accounted for, such that the Maxwell time $\tau = \eta E^{-1}$ of FastIsostasy
is comparable to that of a 3D GIA model. This is done by introducing two correction factors. First, one of the underlying
assumptions made by Cathles (1975) is that the mantle is incompressible, i.e. $\nu^i = 0.5$ is assumed. In reality, the mantle is

however a compressible medium with $\nu^c \simeq 0.28$. We now look for η^i, the viscosity that has to be used in the incompressible

560 case in order to match the Maxwell time of the compressible case. By introducing the shear modulus $G = E\left(2\left(1+\nu\right)\right)^{-1}$, we

obtain:

$$\frac{\eta^i}{2\,G\left(1+\nu^i\right)} \;=\; \frac{\eta^c}{2\,G\left(1+\nu^c\right)} \tag{A1}$$

$$\Leftrightarrow \eta^i \;=\; \frac{1+\nu^i}{1+\nu^c}\,\eta^c = \alpha^c\,\eta^c. \tag{A2}$$

In essence, this means that compressible mediums have a longer relaxation time and that we need to slightly increase the

565 viscosity values for the incompressible case to render this.

Second, both the shear modulus and the viscosity depend on the temperature of the medium. For instance, a positive temperature anomaly in the mantle leads to a negative anomaly of both viscosity and shear modulus. This means that the decrease of the Maxwell time due to the decrease of viscosity is somewhat compensated by the decrease in shear modulus. We have chosen to compute this scaling by calibrating FastIsostasy to results of a 3D GIA model:

570 $$\eta = \exp\left(\log_{10}\left(\frac{\eta_0}{\eta^i}\right)\right)\eta^i = \alpha^G(\eta^i)\,\eta^i, \tag{A3}$$

with $\eta_0 = 10^{21}\,\mathrm{Pa\,s}$ the calibration constant used throughout this work. We thus obtain a relation between the viscosity η^c, inferred from seismic measurements, and the corrected effective viscosity η, ultimately used in FastIsostasy:

$$\eta = \alpha^G\,\alpha^c\,\eta^c = \alpha\,\eta^c. \tag{A4}$$

If the depth dimension is lumped according to Eq. 18, then the viscosity field η_1^{eff}, representing the compound of layers from

575 $l = 1$ to $l = L$, is used for η^c.

Appendix B: Additional figures
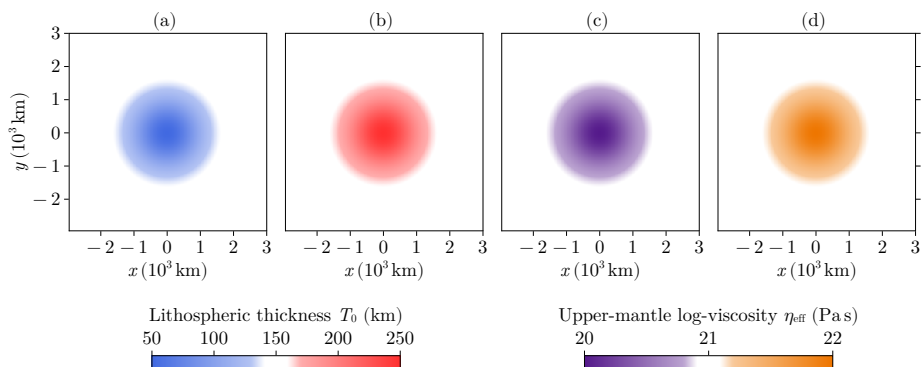
Figure A1. Gaussian-shaped LV for (a) a lithospheric thinning, (b) a lithospheric thickening, (c) a viscosity decrease and (d) a viscosity decrease towards the centre of the domain.
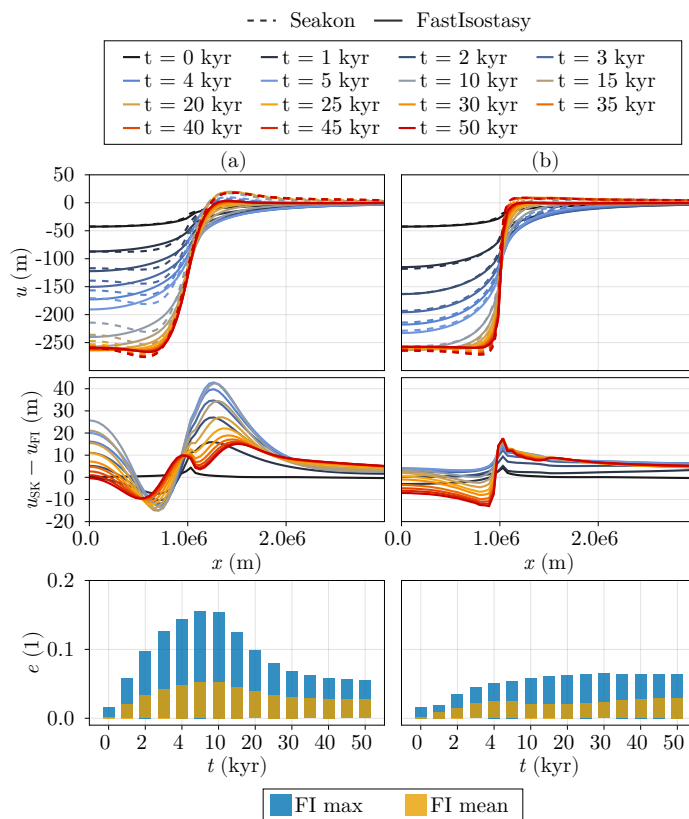
Figure A2. Comparison of FastIsostasy and Seakon for (a) a layered mantle with homogeneous and (b) the absence of any lithosphere.
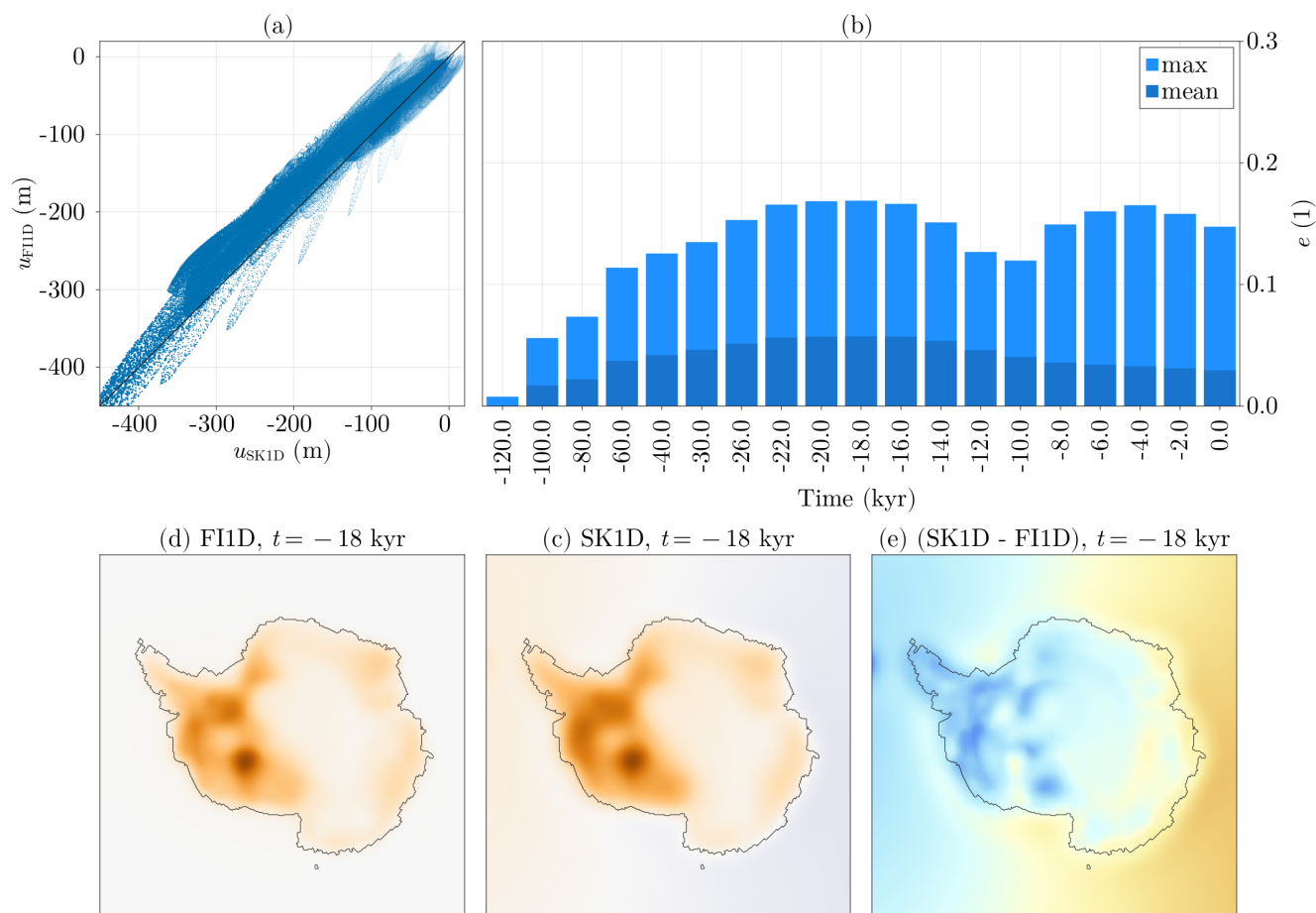
Figure A3. Comparison of SK1D and FI1D, following glacial cycle loading from ICE6G_D. (a) Displacements at all time steps of u_{FI1D} versus u_{SK1D}, for cells that are ice-covered at LGM, visualised by the black contour in panels (c-h). (b) Mean and maximal errors of u_{FI1D} with respect to u_{SK1D} over time. (c-e) Displacement of FI1D, SK1D and their differences for the time step of maximal error.

Author contributions. J.S-J. conceptually developed FastIsostasy as well as its Julia version. The Fortran one was developed by M.M., with contributions from A.R. and J.S-J. The Seakon simulations were performed by K.L., who, along with J.X.M. also provided insights on 3D GIA modelling for the purposes of this manuscript. This manuscript was prepared by J.S-J. with contributions from all co-authors.

580 *Competing interests.* The authors declare no competing interests.

Acknowledgements. We would like to thank Ed Bueler and Constantine Khroulev for the helpful email exchange. Their openly accessible implementations of ELVA, available at https://github.com/pism and https://github.com/bueler/fast-earth, greatly eased the initial phase of FastIsostasy's development and inspired its name. We'd also like to thank Douglas Wiens, Ana Negredo and Javier Fullea for providing valuable comments and/or data.

Financial support. J.S-J. is funded by CriticalEarth, grant no. 956170, an H2020 Research Infrastructure of the European Commission. A.R. received funding from the European Union (ERC, FORCLIMA, 101044247). J.A-S. is funded by the Spanish Ministry of Science and Innovation (project MARINE, grant no. PID2020-117768RB-I00).

590 **References**

Accardo, N. J., Wiens, D. A., Hernandez, S., Aster, R. C., Nyblade, A., Huerta, A., Anandakrishnan, S., Wilson, T., Heeszel, D. S., and
      Dalziel, I. W. D.: Upper mantle seismic anisotropy beneath the West Antarctic Rift System and surrounding region from shear wave
      splitting analysis, Geophysical Journal International, 198, 414–429, https://doi.org/10.1093/gji/ggu117, 2014.

Adhikari, S., Ivins, E. R., Larour, E., Seroussi, H., Morlighem, M., and Nowicki, S.: Future Antarctic bed topography and its implications
595   for ice sheet dynamics, Solid Earth, 5, 569–584, https://doi.org/10.5194/se-5-569-2014, 2014.

Amante, C. and Eakins, B. E.: ETOPO1 1 arc-minute global relief model: procedure, data sources and analysis, Tech. rep., NOAA, 2009.

Argus, D. F., Peltier, W. R., Drummond, R., and Moore, A. W.: The Antarctica component of postglacial rebound model ICE-6G_C (VM5a)
      based on GPS positioning, exposure age dating of ice thicknesses, and relative sea level histories, Geophysical Journal International, 198,
      537–563, https://doi.org/10.1093/gji/ggu140, 2014.

600 Austermann, J., Hoggard, M. J., Latychev, K., Richards, F. D., and Mitrovica, J. X.: The effect of lateral variations in Earth structure on Last
      Interglacial sea level, Geophysical Journal International, 227, 1938–1960, https://doi.org/10.1093/gji/ggab289, 2021.

Bagge, M., Klemann, V., Steinberger, B., Latinović, M., and Thomas, M.: Glacial-Isostatic Adjustment Models Using Geodynamically
      Constrained 3D Earth Structures, Geochemistry, Geophysics, Geosystems, 22, https://doi.org/10.1029/2021GC009853, 2021.

Barletta, V. R., Bevis, M., Smith, B. E., Wilson, T., Brown, A., Bordoni, A., Willis, M., Khan, S. A., Rovira-Navarro, M., Dalziel, I., Smalley,
605   R., Kendrick, E., Konfal, S., Caccamise, D. J., Aster, R. C., Nyblade, A., and Wiens, D. A.: Observed rapid bedrock uplift in Amundsen
      Sea Embayment promotes ice-sheet stability, Science, 360, 1335–1339, https://doi.org/10.1126/science.aao1447, 2018.

Beghein, C., Trampert, J., and van Heijst, H. J.: Radial anisotropy in seismic reference models of the mantle: ANISOTROPY IN MANTLE
      MODELS, Journal of Geophysical Research: Solid Earth, 111, https://doi.org/10.1029/2005JB003728, 2006.

Behrendt, J. C.: Crustal and lithospheric structure of the West Antarctic Rift System from geophysical investigations — a review, Global and
610   Planetary Change, 1999.

Besard, T., Churavy, V., Edelman, A., and Sutter, B. D.: Rapid software prototyping for heterogeneous and distributed platforms, Advances
      in Engineering Software, 132, 29–46, https://doi.org/10.1016/j.advengsoft.2019.02.002, 2019a.

Besard, T., Foket, C., and De Sutter, B.: Effective Extensible Programming: Unleashing Julia on GPUs, IEEE Transactions on Parallel and
      Distributed Systems, 30, 827–841, https://doi.org/10.1109/TPDS.2018.2872064, 2019b.

615 Bezanson, J., Edelman, A., Karpinski, S., and Shah, V. B.: Julia: A Fresh Approach to Numerical Computing, SIAM Review, 59, 65–98,
      https://doi.org/10.1137/141000671, 2017.

Bueler, E., Lingle, C. S., and Brown, J.: Fast computation of a viscoelastic deformable Earth model for ice-sheet simulations, Annals of
      Glaciology, 46, 97–105, https://doi.org/10.3189/172756407782871567, 2007.

Cathles, L. M.: Viscosity of the Earth's Mantle, Princeton University Press, 1975.

620 Cogley, J. G.: Area of the Ocean, Marine Geodesy, 35, 379–388, https://doi.org/10.1080/01490419.2012.709476, 2012.

Coulon, V., Bulthuis, K., Whitehouse, P. L., Sun, S., Haubner, K., Zipf, L., and Pattyn, F.: Contrasting Response of West and East Antarctic
      Ice Sheets to Glacial Isostatic Adjustment, Journal of Geophysical Research: Earth Surface, 126, https://doi.org/10.1029/2020JF006003,
      2021.

Dziewonski, A. M. and Anderson, D. L.: Preliminary Earth Model, Physics of the Earth and Planetary Interiors, 25, 297–356, 1981.

625 Farrell, W. E.: Deformation of the Earth by surface loads, Reviews of Geophysics, 10, 761, https://doi.org/10.1029/RG010i003p00761, 1972.

Farrell, W. E. and Clark, J. A.: On Postglacial Sea Level, Geophysical Journal of the Royal Astronomical Society, 46, 647–667, https://doi.org/10.1111/j.1365-246X.1976.tb01252.x, 1976.

Fretwell, P., Pritchard, H. D., Vaughan, D. G., Bamber, J. L., Barrand, N. E., Bell, R., Bianchi, C., Bingham, R. G., Blankenship, D. D.,
Casassa, G., Catania, G., Callens, D., Conway, H., Cook, A. J., Corr, H. F. J., Damaske, D., Damm, V., Ferraccioli, F., Forsberg, R., Fujita,
S., Gim, Y., Gogineni, P., Griggs, J. A., Hindmarsh, R. C. A., Holmlund, P., Holt, J. W., Jacobel, R. W., Jenkins, A., Jokat, W., Jordan,
T., King, E. C., Kohler, J., Krabill, W., Riger-Kusk, M., Langley, K. A., Leitchenkov, G., Leuschen, C., Luyendyk, B. P., Matsuoka, K.,
Mouginot, J., Nitsche, F. O., Nogi, Y., Nost, O. A., Popov, S. V., Rignot, E., Rippin, D. M., Rivera, A., Roberts, J., Ross, N., Siegert, M. J.,
Smith, A. M., Steinhage, D., Studinger, M., Sun, B., Tinto, B. K., Welch, B. C., Wilson, D., Young, D. A., Xiangbin, C., and Zirizzotti,
A.: Bedmap2: improved ice bed, surface and thickness datasets for Antarctica, The Cryosphere, 7, 375–393, https://doi.org/10.5194/tc-7-
375-2013, 2013.

Frigo, M. and Johnson, S.: The Design and Implementation of FFTW3, Proceedings of the IEEE, 93, 216–231,
https://doi.org/10.1109/JPROC.2004.840301, 2005.

Garbe, J., Albrecht, T., Levermann, A., Donges, J. F., and Winkelmann, R.: The hysteresis of the Antarctic Ice Sheet, Nature, 585, 538–544,
https://doi.org/10.1038/s41586-020-2727-5, 2020.

Gasperini, P., Dal Forno, G., and Boschi, E.: Linear or non-linear rheology in the Earth's mantle: the prevalence of power-law creep in
the postglacial isostatic readjustment of Laurentia, Geophysical Journal International, 157, 1297–1302, https://doi.org/10.1111/j.1365-
246X.2004.02319.x, 2004.

Goelzer, H., Coulon, V., Pattyn, F., de Boer, B., and van de Wal, R.: Brief communication: On calculating the sea-level contribution in marine
ice-sheet models, The Cryosphere, 14, 833–840, https://doi.org/10.5194/tc-14-833-2020, 2020.

Gomez, N., Mitrovica, J. X., Huybers, P., and Clark, P. U.: Sea level as a stabilizing factor for marine-ice-sheet grounding lines, Nature
Geoscience, 3, 850–853, https://doi.org/10.1038/ngeo1012, 2010.

Gomez, N., Pollard, D., Mitrovica, J. X., Huybers, P., and Clark, P. U.: Evolution of a coupled marine ice sheet-sea level model, Journal of
Geophysical Research: Earth Surface, 117, https://doi.org/10.1029/2011JF002128, 2012.

Gomez, N., Pollard, D., and Holland, D.: Sea-level feedback lowers projections of future Antarctic Ice-Sheet mass loss, Nature Communi-
cations, 6, 8798, https://doi.org/10.1038/ncomms9798, 2015.

Gomez, N., Latychev, K., and Pollard, D.: A Coupled Ice Sheet–Sea Level Model Incorporating 3D Earth Structure: Variations in Antarctica
during the Last Deglacial Retreat, Journal of Climate, 31, 4041–4054, https://doi.org/10.1175/JCLI-D-17-0352.1, 2018.

Gudmundsson, G. H., Krug, J., Durand, G., Favier, L., and Gagliardini, O.: The stability of grounding lines on retrograde slopes, The
Cryosphere, 6, 1497–1505, https://doi.org/10.5194/tc-6-1497-2012, 2012.

Ivins, E. R., Caron, L., Adhikari, S., and Larour, E.: Notes on a compressible extended Burgers model of rheology, Geophysical Journal
International, 228, 1975–1991, https://doi.org/10.1093/gji/ggab452, 2021.

Ivins, E. R., van der Wal, W., Wiens, D. A., Lloyd, A. J., and Caron, L.: Antarctic upper mantle rheology, Geological Society, London,
Memoirs, 56, M56–2020–19, https://doi.org/10.1144/M56-2020-19, 2022.

Kendall, R. A., Mitrovica, J. X., and Milne, G. A.: On post-glacial sea level - II. Numerical formulation and comparative results on spherically
symmetric models, Geophysical Journal International, 161, 679–706, https://doi.org/10.1111/j.1365-246X.2005.02553.x, 2005.

Klemann, V., Martinec, Z., and Ivins, E. R.: Glacial isostasy and plate motion, Journal of Geodynamics, 46, 95–103,
https://doi.org/10.1016/j.jog.2008.04.005, 2008.

Konrad, H., Thoma, M., Sasgen, I., Klemann, V., Grosfeld, K., Barbi, D., and Martinec, Z.: The Deformational Response of a Viscoelastic Solid Earth Model Coupled to a Thermomechanical Ice Sheet Model, Surveys in Geophysics, 35, 1441–1458, https://doi.org/10.1007/s10712-013-9257-8, 2014.

Konrad, H., Sasgen, I., Pollard, D., and Klemann, V.: Potential of the solid-Earth response for limiting long-term West Antarctic Ice Sheet retreat in a warming climate, Earth and Planetary Science Letters, 432, 254–264, https://doi.org/10.1016/j.epsl.2015.10.008, 2015.

Konrad, H., Sasgen, I., Klemann, V., Thoma, M., Grosfeld, K., and Martinec, Z.: Sensitivity of Grounding-Line Dynamics to Viscoelastic Deformation of the Solid-Earth in an Idealized Scenario, Polarforschung; 85, https://doi.org/10.2312/POLFOR.2016.005, publisher: Bibliothek Wissenschaftspark Albert Einstein, 2016.

Kulp, S. A. and Strauss, B. H.: New elevation data triple estimates of global vulnerability to sea-level rise and coastal flooding, Nature Communications, 10, 4844, https://doi.org/10.1038/s41467-019-12808-z, 2019.

Latychev, K., Mitrovica, J. X., Tromp, J., Tamisiea, M. E., Komatitsch, D., and Christara, C. C.: Glacial isostatic adjustment on 3-D Earth models: a finite-volume formulation, Geophysical Journal International, 161, 421–444, https://doi.org/10.1111/j.1365-246X.2005.02536.x, 2005.

Le Meur, E. and Huybrechts, P.: A comparison of different ways of dealing with isostasy: examples from modelling the Antarctic ice sheet during the last glacial cycle, Annals of Glaciology, 23, 309–317, https://doi.org/10.3189/S0260305500013586, 1996.

Lingle, C. S. and Clark, J. A.: A numerical model of interactions between a marine ice sheet and the solid earth: Application to a West Antarctic ice stream, Journal of Geophysical Research, 90, 1100, https://doi.org/10.1029/JC090iC01p01100, 1985.

Lloyd, A. J., Wiens, D. A., Nyblade, A. A., Anandakrishnan, S., Aster, R. C., Huerta, A. D., Wilson, T. J., Dalziel, I. W. D., Shore, P. J., and Zhao, D.: A seismic transect across West Antarctica: Evidence for mantle thermal anomalies beneath the Bentley Subglacial Trench and the Marie Byrd Land Dome, Journal of Geophysical Research: Solid Earth, 120, 8439–8460, https://doi.org/10.1002/2015JB012455, 2015.

Lloyd, A. J., Wiens, D. A., Zhu, H., Tromp, J., Nyblade, A. A., Aster, R. C., Hansen, S. E., Dalziel, I. W. D., Wilson, T., Ivins, E. R., and O'Donnell, J. P.: Seismic Structure of the Antarctic Upper Mantle Imaged with Adjoint Tomography, Journal of Geophysical Research: Solid Earth, 125, 2019JB017 823, https://doi.org/10.1029/2019JB017823, 2020.

Martinec, Z.: Spectral-finite element approach to three-dimensional viscoelastic relaxation in a spherical earth, Geophysical Journal International, 142, 117–141, https://doi.org/10.1046/j.1365-246x.2000.00138.x, 2000.

Martinec, Z., Klemann, V., van der Wal, W., Riva, R. E. M., Spada, G., Sun, Y., Melini, D., Kachuck, S. B., Barletta, V., Simon, K., A, G., and James, T. S.: A benchmark study of numerical implementations of the sea level equation in GIA modelling, Geophysical Journal International, 215, 389–414, https://doi.org/10.1093/gji/ggy280, 2018.

Mitrovica, J. X. and Milne, G. A.: On post-glacial sea level: I. General theory, Geophysical Journal International, 154, 253–267, https://doi.org/10.1046/j.1365-246X.2003.01942.x, 2003.

Mitrovica, J. X., Milne, G. A., and Davis, J. L.: Glacial isostatic adjustment on a rotating earth, Geophysical Journal International, 147, 562–578, https://doi.org/10.1046/j.1365-246x.2001.01550.x, 2001.

Mitrovica, J. X., Gomez, N., and Clark, P. U.: The Sea-Level Fingerprint of West Antarctic Collapse, Science, 323, 753–753, https://doi.org/10.1126/science.1166510, 2009.

Morelli, A. and Danesi, S.: Seismological imaging of the Antarctic continental lithosphere: a review, Global and Planetary Change, 42, 155–165, https://doi.org/10.1016/j.gloplacha.2003.12.005, 2004.

700 Morlighem, M., Rignot, E., Binder, T., Blankenship, D., Drews, R., Eagles, G., Eisen, O., Ferraccioli, F., Forsberg, R., Fretwell, P., Goel, V., Greenbaum, J. S., Gudmundsson, H., Guo, J., Helm, V., Hofstede, C., Howat, I., Humbert, A., Jokat, W., Karlsson, N. B., Lee, W. S., Matsuoka, K., Millan, R., Mouginot, J., Paden, J., Pattyn, F., Roberts, J., Rosier, S., Ruppel, A., Seroussi, H., Smith, E. C., Steinhage, D., Sun, B., Broeke, M. R. V. D., Ommen, T. D. V., Wessem, M. V., and Young, D. A.: Deep glacial troughs and stabilizing ridges unveiled beneath the margins of the Antarctic ice sheet, Nature Geoscience, 13, 132–137, https://doi.org/10.1038/s41561-019-0510-8, 2020.

705 Nield, G. A., Barletta, V. R., Bordoni, A., King, M. A., Whitehouse, P. L., Clarke, P. J., Domack, E., Scambos, T. A., and Berthier, E.: Rapid bedrock uplift in the Antarctic Peninsula explained by viscoelastic response to recent ice unloading, Earth and Planetary Science Letters, 397, 32–41, https://doi.org/10.1016/j.epsl.2014.04.019, 2014.

Pan, L., Powell, E. M., Latychev, K., Mitrovica, J. X., Creveling, Gomez, N., Hoggard, M. J., and Clark, P. J.: Rapid postglacial rebound amplifies global sea level rise following West Antarctic Ice Sheet collapse, SCIENCE ADVANCES, 2021.

710 Pan, L., Milne, G. A., Latychev, K., Goldberg, S. L., Austermann, J., Hoggard, M. J., and Mitrovica, J. X.: The influence of lateral Earth structure on inferences of global ice volume during the Last Glacial Maximum, Quaternary Science Reviews, 290, 107 644, https://doi.org/10.1016/j.quascirev.2022.107644, 2022.

Peltier, W. R., Argus, D. F., and Drummond, R.: Space geodesy constrains ice age terminal deglaciation: The global ICE-6G_C (VM5a) model, Journal of Geophysical Research: Solid Earth, 120, 450–487, https://doi.org/10.1002/2014JB011176, 2015.

715 Peltier, W. R., Argus, D. F., and Drummond, R.: Comment on "An Assessment of the ICE-6G_C (VM5a) Glacial Isostatic Adjustment Model" by Purcell et al., Journal of Geophysical Research: Solid Earth, 123, 2019–2028, https://doi.org/10.1002/2016JB013844, 2018.

Purcell, A., Tregoning, P., and Dehecq, A.: An assessment of the *ICE6G_C(VM5a)* glacial isostatic adjustment model, Journal of Geophysical Research: Solid Earth, 121, 3939–3950, https://doi.org/10.1002/2015JB012742, 2016.

Rackauckas, C. and Nie, Q.: DifferentialEquations.jl – A Performant and Feature-Rich Ecosystem for Solving Differential Equations in Julia, 720 Journal of Open Research Software, 5, 15, https://doi.org/10.5334/jors.151, 2017.

Seroussi, H., Nowicki, S., Payne, A. J., Goelzer, H., Lipscomb, W. H., Abe-Ouchi, A., Agosta, C., Albrecht, T., Asay-Davis, X., Barthel, A., Calov, R., Cullather, R., Dumas, C., Galton-Fenzi, B. K., Gladstone, R., Golledge, N. R., Gregory, J. M., Greve, R., Hattermann, T., Hoffman, M. J., Humbert, A., Huybrechts, P., Jourdain, N. C., Kleiner, T., Larour, E., Leguy, G. R., Lowry, D. P., Little, C. M., Morlighem, M., Pattyn, F., Pelle, T., Price, S. F., Quiquet, A., Reese, R., Schlegel, N.-J., Shepherd, A., Simon, E., Smith, R. S., Straneo, F., Sun, S., 725 Trusel, L. D., Van Breedam, J., Van De Wal, R. S. W., Winkelmann, R., Zhao, C., Zhang, T., and Zwinger, T.: ISMIP6 Antarctica: a multi-model ensemble of the Antarctic ice sheet evolution over the 21st century, The Cryosphere, 14, 3033–3070, https://doi.org/10.5194/tc-14-3033-2020, 2020.

Spada, G. and Melini, D.: SELEN4 (SELEN version 4.0): a Fortran program for solving the gravitationally and topographically self-consistent sea-level equation in glacial isostatic adjustment modeling, Geoscientific Model Development, 12, 5055–5075, 730 https://doi.org/10.5194/gmd-12-5055-2019, 2019.

Spada, G., Barletta, V. R., Klemann, V., Riva, R. E., Martinec, Z., Gasperini, P., Lund, B., Wolf, D., Vermeersen, L. L. A., and King, M. A.: A benchmark study for glacial isostatic adjustment codes: A GIA benchmark study, Geophysical Journal International, 185, 106–132, https://doi.org/10.1111/j.1365-246X.2011.04952.x, 2011.

Van Calcar, C. J., Van De Wal, R. S. W., Blank, B., De Boer, B., and Van Der Wal, W.: Simulation of a fully coupled 3D glacial iso-735 static adjustment – ice sheet model for the Antarctic ice sheet over a glacial cycle, Geoscientific Model Development, 16, 5473–5492, https://doi.org/10.5194/gmd-16-5473-2023, 2023.

van der Wal, W., Wu, P., Wang, H., and Sideris, M. G.: Sea levels and uplift rate from composite rheology in glacial isostatic adjustment modeling, Journal of Geodynamics, 50, 38–48, https://doi.org/10.1016/j.jog.2010.01.006, 2010.

van der Wal, W., Whitehouse, P. L., and Schrama, E. J. O.: Effect of GIA models with 3D composite mantle viscosity on GRACE mass
740 balance estimates for Antarctica, Earth and Planetary Science Letters, 414, 134–143, https://doi.org/10.1016/j.epsl.2015.01.001, 2015.

Ventsel, E. and Krauthammer, T.: Thin Plates and Shells: Theory, Analysis, and Applications, CRC Press, Boca Raton, 1st edition edn., ISBN 978-0-429-22131-6, 2001.

Wan, J. X. W., Gomez, N., Latychev, K., and Han, H. K.: Resolving glacial isostatic adjustment (GIA) in response to modern and future ice loss at marine grounding lines in West Antarctica, The Cryosphere, 16, 2203–2223, https://doi.org/10.5194/tc-16-2203-2022, 2022.

745 Weerdesteijn, M. F. M., Naliboff, J. B., Conrad, C. P., Reusen, J. M., Steffen, R., Heister, T., and Zhang, J.: Modeling Viscoelastic Solid Earth Deformation Due To Ice Age and Contemporary Glacial Mass Changes in ASPECT, Geochemistry, Geophysics, Geosystems, 24, e2022GC010 813, https://doi.org/10.1029/2022GC010813, 2023.

Whitehouse, P. L., Gomez, N., King, M. A., and Wiens, D. A.: Solid Earth change and the evolution of the Antarctic Ice Sheet, Nature Communications, 10, 503, https://doi.org/10.1038/s41467-018-08068-y, 2019.

750 Wiens, D. A., Shen, W., and Lloyd, A. J.: The seismic structure of the Antarctic upper mantle, Geological Society, London, Memoirs, 56, M56–2020–18, https://doi.org/10.1144/M56-2020-18, 2022.

Wu, P.: Using commercial finite element packages for the study of earth deformations, sea levels and the state of stress, Geophysical Journal International, 158, 401–408, https://doi.org/10.1111/j.1365-246X.2004.02338.x, 2004.

Wu, P. and Wang, H.: Effects of mode coupling and location of rotational axis on glacial induced rotational deformation in a laterally
755 heterogeneous viscoelastic earth, Geophysical Journal International, 167, 853–859, https://doi.org/10.1111/j.1365-246X.2006.03103.x, 2006.

Zhong, S., Kang, K., A, G., and Qin, C.: CitcomSVE: A Three-Dimensional Finite Element Software Package for Modeling Planetary Mantle's Viscoelastic Deformation in Response to Surface and Tidal Loads, Geochemistry, Geophysics, Geosystems, 23, e2022GC010 359, https://doi.org/10.1029/2022GC010359, 2022.